Energy Conversion and Management 293 (2023) 117436

Contents lists available at ScienceDirect

Energy Conversion and Management

journal homepage: www.elsevier.com/locate/enconman

Modeling a solar pressurized volumetric receiver integrated in a parabolic dish: Off-design heat transfers, temperatures, and efficiencies

J. García Ferrero [a,*], R.P. Merchán [a], M.J. Santos [a], A. Medina [a], A. Calvo Hernández [a], P. Canhoto [b], A. Giostri [c]

[a] Department of Applied Physics and Institute of Fundamental Physics and Mathematics (IUFFYM), Universidad de Salamanca, 37008 Salamanca, Spain
[b] Instituto de Ciências da Terra, Universidade de Évora, Rua Romão Ramalho 59, 7000-671 Évora, Portugal
[c] Group of Energy Conversion Systems, Politecnico di Milano, Via Lambruschini 4, 20156, Milan, Italy

ARTICLE INFO

Keywords:
Concentrated solar power
Solar receiver
Parabolic dish
Ray tracing optical models
Heat transfer and losses
Realistic meteorological data

ABSTRACT

Concentrated solar power plants are commonly recognized as one of the most attractive options within carbon-free power generation technologies because of their high efficiency and feasible hybridization and/or storage implementation. In this work, a complete heat transfer analysis for an air volumetric receiver coupled to a parabolic dish focused on distributed generation (in the range of kWe) is carried out. It includes most relevant heat losses. Dish collector optical efficiency is computed by means of a ray-tracing software while the thermal performance of the solar receiver is modeled under steady-state conditions using a comprehensive set of equations with a clear physical origin and meaning. Detailed information on the temperatures and heat transfers along the different inner and outer receiver zones are computed with a built from scratch in-house code programmed in Mathematica®. The model considers the main losses from convection, conduction and radiation and through the surrounding insulator. The resulting thermal efficiency mainly depends on the incoming solar irradiance at the glass window, the receiver geometry and the type of materials considered, as well as on the ambient temperature. Explicit numerical results are given at two locations under different meteorological conditions. Optical efficiencies reach values of about 84%. For irradiance values around 800–900 W/m^2, at the receiver outlet, air can reach temperatures of about 1200 K and receiver thermal efficiency is over 80%. It is expected that this model (precise but not too expensive from the computational viewpoint) could help to identify the main efficiency bottlenecks, paving the way for optimization when designing this type of concentrated solar plants through further coupling with a power block, as Brayton or other cycles.

1. Introduction

Key elements in any concentrated solar power (CSP) system are the solar collector and the solar receiver. The solar collector is an optical subsystem designed to collect and concentrate in an efficient way the direct solar irradiance towards the solar receiver. It is characterized by an optical efficiency that measures the fraction of solar power that effectively reaches the solar receiver window. Nowadays, most research works make use of ray tracing Monte Carlo software to compute its optical efficiency [1]. Monte Carlo methods applied to solar ray tracing are based upon the generation of a huge number of photons over the aperture area of the solar collector [2]. The pathway of the photons is built through reflection laws and it is computed if they strike on the receiver aperture. From this, estimations of the optical efficiency of the collector with a good precision and also of the distribution of incident energy flux onto the absorbing surface [3] can be calculated.

The solar receiver can be considered as a special type of heat exchanger with the aim of converting the input direct solar irradiance into heat. The receiver thermal efficiency is essential to obtain high efficiency in the overall CSP plant and so, to increase commercial interest. Many experimental or simulation studies have been conducted in order to propose optimized designs to account for the high complexity of the heat transfer processes in the solar receiver, as it can be seen in the comprehensive review by Sedighi et al. [4].

An interesting application of CSP systems is the possibility of producing distributed electricity at the scale of kW$_e$, close to the consumption place. Solar dishes, for instance, are capable to perform this task easier than other systems because of their modularity [1]. A collecting parabolic dish reflects the input solar radiation into a solar receiver located at parabola focus, where it is transferred to a fluid running a thermodynamic cycle as power block [5]. Particularly,

* Corresponding author.
E-mail addresses: jgferrero@usal.es (J. García Ferrero), rpmerchan@usal.es (R.P. Merchán), smjesus@usal.es (M.J. Santos), amd385@usal.es (A. Medina), anca@usal.es (A. Calvo Hernández), canhoto@uevora.pt (P. Canhoto), andrea.giostri@polimi.it (A. Giostri).

https://doi.org/10.1016/j.enconman.2023.117436
Received 17 May 2023; Received in revised form 17 July 2023; Accepted 18 July 2023
Available online 4 August 2023

Nomenclature

Symbols & Units

A	Area (m^2)
c_p	Isobaric specific heat capacity (J/kg K)
f_p	Friction factor –
g	Acceleration of gravity (m/s^2)
h	Convective heat transfer coefficient (W/m^2 K)
$\bar{h}$	Specific enthalpy (J/kg)
I_b	Solar radiation power (W)
k_{air}	Air thermal conductivity (W/m K)
$\bar{k}$	Average thermal conductivity (W/m K)
$\dot{m}$	Mass flow (kg/s)
Nu	Nusselt number –
P	Power (W)
Pr	Prandlt number –
$\dot{Q}$	Thermal power (W)
Ra	Rayleigh number –
Re	Reynolds number –
R_{th}	Thermal resistance (m^2 K/W)
U	Global conduction, convection and radiation heat transfer coefficient (W/m^2 K)
u	Air superficial velocity (module) (m/s)

Greek symbols

β	Coefficient of volumetric expansion (K^{-1})
η_{opt}	Optical efficiency –
$\eta_{th,rcv}$	Thermal efficiency –
μ	Dynamic viscosity (Pa s)
ρ	Fluid density (kg/m^3)

Acronyms

CFD	Computational Fluid Dynamics
CSP	Concentrated Solar Power
DNI	Direct Normal Irradiance
HTF	Heat Transfer Fluid
LMTD	Logarithmic Mean Temperature Difference
MCRT	Monte-Carlo Ray Tracer
PDC	Parabolic Dish Collector

Brayton cycles are being investigated due to their promising features as high efficiency, versatility, compactness, and possibility to integrate hybridization or storage schemes [6]. Requirements for solar receivers designed to operate together with Brayton cycles include the necessity to operate at high temperatures (over about 800 °C) and relatively high pressures (up to 20 bar) [7].

Feasible hybridization arrangements and control strategies for dish-Brayton systems have been reported by Wang et al. [8], while Mohammadi and Mehrpooya [9] analyzed the possible integration with energy storage using compressed air technology. Detailed and novel results along this storage research line have been reported very recently presenting improved technology used in the efficient utilization of renewable energy to get carbon neutrality. So, simulation analyses were carried out in terms of solid–liquid interface evolution, melting front formation, temperature and flow field, and energy storage capacity in a latent heat filled with four different system providing a data bench for validating the numerical models by Zhao et al. [10]. Also, a flip mechanism was used to reduce the proportion of high-temperature phase change material in the melting process within the work by Fangfei et al. [11].

Pressurized volumetric receivers can be compact and reach large efficiency (78% to 80%) at large temperatures and pressures, adequate for Brayton cycles [7]. Moreover, can operate with gases different from air, as helium, argon, nitrogen or CO_2. Their design continue being a challenge nowadays in order to set the basis for new evolutions of CSP systems, increasingly interesting from an economic perspective [6]. These receivers are usually closed with a quartz glass window that can reach temperatures about 1200 °C and it is cooled by the thermal fluid itself or through an extra cooling system [12]. Behind the glass, there is a cavity containing a porous media, the absorber, that is directly impinged by solar radiation. The gas flows through its pores getting a high temperature. Foam can be metallic or ceramic [13]. The first are more economic and can reach temperatures about 1450 °C, for instance with Nickel compounds. Other advantages of metal foams include high porosity and specific surface area, as well as, high mechanical strength.

Outer walls of the receivers are usually thermally isolated from the ambient to minimize heat losses. Aluminum silicate is a usual material with a low thermal conductivity (around 0.06 W/(m.K)) [14]. Bellos et al. [15] have reviewed the most recent technologies and advances on cavity receiver designs for solar dish concentrators. The influence of different geometries and materials for cavity receivers specially focused for solar dish applications has been analyzed by Kasaeian et al. [16].

Studies and analysis of receivers for solar dish utilization include experiments and simulations at different levels. Zhu et al. [12,14] performed both studies for an own design. The experimental study was conducted at Hangzhou, China, and consisted of a compressor, a dish and a receiver with a Ni foam absorber [12]. Variations with time of different parameters as energy and exergy efficiencies, heat losses, temperatures and pressures were performed at real solar conditions in a period with approximately constant direct normal irradiance (DNI). Subsequently, a simplified stationary model for heat transfer in receiver zones was presented. A good agreement was obtained between experimental and calculated receiver efficiency (with values about 82%) [14].

At a different level of refinement, Wang et al. [17] developed a computational fluid dynamics (CFD) model that was validated against experimental measures. A SiC (silicon carbide) absorber was utilized and different porous parameters were analyzed. Maximum temperatures of the outlet air slightly exceeded 1000 K. Solar to thermal efficiencies over 63% were obtained, including optical efficiency and thermal losses. A recent analysis of the thermal and mechanical performance of the same kind of absorber (silicon carbide) was reported and calculations through CFD simulations for the temperature distribution along the absorber axis, pressure drops, the failure index, and of the incident solar heat flux were presented by Sharma and Talukdar [18]. By means of CFD and ray tracing methods heat losses of tubular cavity receiver for solar dishes including wind effects have been calculated by Craig et al. [19].

Recent international projects such as OMSoP [20] have proved the feasibility of solar dishes coupled to Brayton cycles at an experimental level by completing a prototype plant but also, have shown the necessity of developing computational models [21] for simulating plant operation at different realistic conditions in order to improve system efficiency, both at design and off-design operation. Particularly, solar collector and solar receiver performance are to be improved in order to advance in the profitability of this technology. In this context, the furthest aim of this work is to accurately predict the thermal efficiency of the system made up of a parabolic dish collector (PDC) and a solar volumetric receiver placed at its focus. A ray-tracing software, Tonatiuh [3], will be employed for an accurate simulation of the PDC optical efficiency and the results processed in a Mathematica® code [22] aiming to their integration into the receiver model equations.

Main focus is devoted to a complete modeling of the volumetric receiver for accurate efficiency estimations. The model developed in this work includes novel features not considered and/or barely touched in previous works, at least to the best of the author's knowledge:

(i) a volumetric (instead of superficial) heat transfer coefficient for the porous media is taken into account; (ii) an additional convective heat exchange at the inner receiver wall is considered; (iii) different temperatures inside and outside the glass window; (iv) losses across the receiver insulator; (v) more accurate expressions for thermal radiation exchanges, and finally (vi) a more complete set of view factors than in previous works have been included explicitly in the modeling through appropriate energy balance equations.

The used methodology combines a parabolic dish optical modeling using Tonatiuh software joined to numerical computations of each of the involved heat transfer (including associated losses) and temperatures at five well delimited different zones of the receiver. The resulting comprehensive set of equations involves a relatively large number of parameters, but all of them are controllable and, more important, with a clear physical origin and meaning, allowing for the analysis of possible bottlenecks. Explicit numerical results for the fluid and surface temperatures in each zone together with results for the optical and thermal receiver efficiencies for different locations and meteorological conditions can be obtained. Thus, the proposed overall model could be used as an alternative/complementary method to CFD analysis that requires an extensive computational effort and additionally the key physical factors affecting global system efficiency are not always easy to extract.

The paper is structured as follows. Next section shows the parabolic dish optical modeling using Tonatiuh software and the detailed analysis of heat transfer processes at the solar volumetric receiver incorporating five well delimited different zones. Submodels are validated in Section 3 and all numerical parameters required to reproduce the results are also compiled in this section and in the corresponding appendices. Section 4 presents explicit numerical results for the fluid and surface temperatures in each zone together with results for the optical and thermal receiver efficiencies for different locations and meteorological conditions. Finally, some conclusions are summarized in Section 5. Appendices contain detailed information for receiver model numerical calculus and additional Tonatiuh validation details.

2. Model and simulations

The basic elements of Tonatiuh software, together with the solar receiver model, are exposed in the following subsections.

2.1. Energy efficiency equation

As it is shown in Eq. (1), the receiver thermal efficiency, $\eta_{th,rcv}$, is the ratio between the heat absorbed by the receiver and the total heat flux impinging at the receiver aperture area:

$$\eta_{th,rcv} = \frac{\dot{Q}_r}{I_b} = \frac{\dot{m}\,(\bar{h}_o - \bar{h}_i)}{\eta_{opt}\,A_d\,\mathrm{DNI}} \tag{1}$$

where $\dot{Q}_r$ stands for the heat flux absorbed by the fluid at the receiver. It can be calculated in terms of the fluid mass flow through the receiver, $\dot{m}$, and the difference between the outlet and inlet fluid-specific enthalpies, $\bar{h}_o$ and $\bar{h}_i$, respectively. I_b is the solar radiation power impinging at the solar receiver window. This parameter can be expressed as the product of the parabolic dish optical efficiency, η_{opt}, dish aperture area, A_d, and direct solar irradiance (DNI) [14,23]. This equation shows how the submodels for the optical behavior of the dish itself and the thermal performance of the receiver are coupled. $\eta_{th,rcv}$ directly depends on the optical efficiency, η_{opt}, apart from the dish aperture area and DNI, which are input parameters. Also $\dot{m}$ is an input parameter related to the operation strategy. It can be constant or time dependent, in the last case to avoid overheating of the receiver or to regulate power output. In our study it will be considered constant (see below). In the next subsections, separate submodels for the dish (to obtain η_{opt}) and the receiver (to obtain essentially $(\bar{h}_o - \bar{h}_i)$) will be presented and afterwards integrated through Eq. (1).

Table 1
Tonatiuh main parameters for simulating a PDC and its receiver.

Tonatiuh optical parameters	
Sunlight properties	
DNI	Direct Normal Irradiance
Sun shape	Buie or Pillow
CSR	Circumsolar ratio for Buie Sun shape distribution
Number of rays (photons)	Number of random photons/rays employed for Monte-Carlo ray tracing
Collector	
ρ_d	Optical mirror reflectivity for parabolic dish
σ_s	Slope error (including 'macro' and 'micro' errors)
A_d	Dish aperture area
D	Dish aperture diameter
ψ	Aperture angle
f_d	Dish focus length
Receiver	
D_g	Receiver (glass window) aperture diameter

2.2. Parabolic dish optical modeling: Tonatiuh software

Tonatiuh is an open-source Monte-Carlo Ray Tracer (MCRT) software [3,24] for the optical simulation of solar concentrating systems. In this work, a PDC and a target surface (receiver) placed at its focus will be simulated. The receiver will be a flat circle, representing the glass window aperture where the photons arrive after being reflected at the PDC surface. In Table 1, the main necessary variables for simulating a concentrating solar system of the type considered are specified. The numerical parameters (dish geometry and materials, Sun parameters, etc.) will differ for validation and for off-design simulations and will be made explicit in subsequent sections.

2.3. Solar volumetric receiver modeling: Heat transfer equations

The solar receiver model presented hereby considers an axially cylindrical pressurized volumetric receiver with a geometrical design as shown in Fig. 1. For validation and numerical applications the design by Zhu et al. [14] will be considered, but the models developed in this paper could be applied to other designs and dimensions in a straightforward manner. Symmetry axis goes through window center and it is normal to the window surface. This kind of receivers are specially interesting for high temperature applications because aperture quartz glasses can reach temperatures quite above 1000°C and receiver thermal efficiency at such conditions can be very high. Usually the heat transfer fluid (HTF) is pressurized air and receiver core is a metal or ceramic foam that will be considered as a uniform medium with a given porosity (zone 4 in Fig. 1).

All the temperatures and heat exchanges involved are included and shown in Fig. 1(a). Fig. 1(b) displays the main geometric parameters considered. The HTF enters the receiver at T_i temperature and crosses different zones until it arrives at the outlet, at temperature T_o. Next, a brief description of all zones involved in heat transfers is given.

- Zone 1: It can be split in two parts: phase $i-1$, and phase $4-o$. The colder air (at temperature T_i) receives heat ($\dot{Q}_1$) from the air which is crossing the receiver outlet, since the latter has a higher temperature (T_o). Thus, the air arrives at Zone 2 at temperature T_1. Due to this heat exchange, the temperature at the receiver exit, T_o, is slightly lower than the air temperature just after crossing the absorber foam (T_4). The heat transfer can be modeled as a heat exchanger with mixed convection and conduction processes.
- Zone 2: There is a heat transfer ($\dot{Q}_2$) through the inner cylinder wall (at temperature T_w) to the air, which rises its temperature from T_1 to T_2. $\dot{Q}_2$ comes from the thermal and visible radiation emitted by the absorber foam and the glass window to the inner cylinder wall.

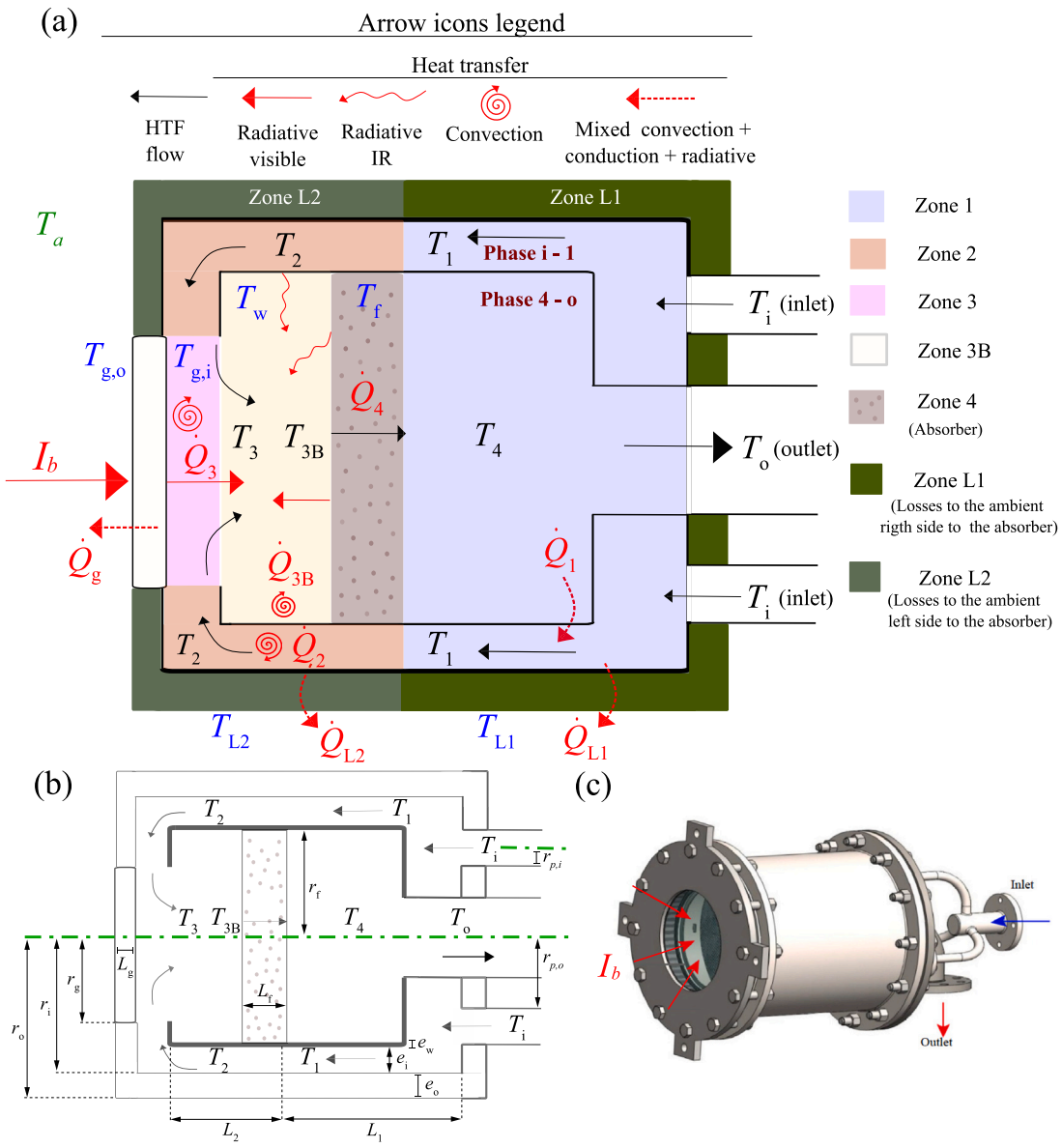

Fig. 1. (a) Scheme of the receiver used for this work [14]. Heat Transfer Fluid (HTF) temperatures (T_i, T_1, T_2, T_3, T_{3B}, T_4 and T_o) are depicted in black. Surfaces temperatures related to glass (inner and outer surfaces), internal wall, absorber foam, front external insulator, and back external insulator ($T_{g,i}$, $T_{g,o}$, T_w, T_f, T_{L1} and T_{L2}, respectively) in blue and ambient temperature (T_a) is depicted in green. Thermal power exchanges ($\dot{Q}_1$, $\dot{Q}_2$, $\dot{Q}_3$, $\dot{Q}_{3B}$, $\dot{Q}_4$, $\dot{Q}_{L1}$, $\dot{Q}_{L2}$ and I_b) are depicted in red. (b) Geometrical parameters used in the heat transfer model of the receiver. (c) 3D image of the receiver.
Source: Taken from Zhu et al. [14].

- Zone 3: The air receives a heat flux $\dot{Q}_3$ by means of convection with the inner glass surface (at temperature $T_{g,i}$). Thus, the air achieves temperature T_3. Besides, the heat balance at the glass window has to be considered. It will be further explained in detail in the following paragraphs.
- Zone 3B: The air exchanges a heat flux, $\dot{Q}_{3B}$, through convection with the inner wall surface (at temperature T_w). Hence, the air arrives at the absorber foam at temperature T_{3B}. $\dot{Q}_{3B}$ influences the energy balance at Zone 2.
- Zone 4: Here, the fluid crosses the absorber foam (at temperature T_f), receiving thus a heat flux $\dot{Q}_4$. In this stage, the air rises its temperature up to T_4. The heat transfer corresponds to a convection with the pores inside the absorber foam.

The previous brief explanation serves as an introduction for simulating the receiver. The equations are exposed in the following paragraphs but first, some considerations should be pointed out:

- A steady-state model is considered. Hence, mass balance equations ($\dot{m}_i = \cdots = \dot{m}_o = \dot{m}$) will be indirectly included within heat balance equations. Additionally, temperatures across the receiver zones will be uniform in each of them.
- Absorber foam (T_f) temperature is considered uniform along the whole material.
- The wall of the inner cylinder is considered a gray body under thermal-balance conditions. Then, its absorptivity (α_w) and emittance (ϵ_w) are equivalent. Note that α_w and ϵ_w will be considered as constant values along the wavelength range. This inner cylinder wall also possesses a uniform temperature T_w.
- The glass thermal radiation transmittance is considered negligible.

Regarding the pressure, it has been considered a global pressure drop of 0.2 bar across the receiver [23]. The following equations describe the volumetric solar receiver model.

2.3.1. Zone 1

The heat exchange in this stage is modeled as sort of heat exchanger. Then, the energy balance can be written as [25]:

$$\dot{Q}_1 = \dot{m}\,\bar{c}_p(T)(T_1 - T_i) + \dot{Q}_{L1} = \dot{m}\,\bar{c}_p(T)(T_4 - T_o) \tag{2}$$

where $\bar{c}_p(T)$ stands for the average isobaric thermal capacity between temperatures T_i and T_1, or between T_4 and T_o. $\bar{c}_p(T)$ is calculated through REFPROP coupled with Mathematica® [22,26] (see Appendix A). $\dot{Q}_{L1}$ stands for the thermal losses through the insulator (Zone L1, see Fig. 1), which will be detailed below. Besides, as a counter-flow heat exchanger, the heat transfer should meet the following relation [25]:

$$\dot{Q}_1 = U_1 A_1 \frac{(T_o - T_i) - (T_4 - T_1)}{\log \frac{(T_o - T_i)}{(T_4 - T_1)}} \tag{3}$$

where U_1 represents a global (conduction and convection) heat transfer coefficient and A_1 stands for the effective Zone 1 area. The global heat transfer coefficient, which is the inverse of the total thermal resistance, can be calculated from [25]:

$$U_1 = R_{th.total}^{-1} = \left(R_{th.conv.1} + R_{th.cond} + R_{th.conv.2}\right)^{-1}$$

$$U_1 = \left[\frac{1}{h_{i1}} + \frac{e_w}{\bar{k}_w(T_{io})} + \frac{1}{h_{4o}}\right]^{-1} \tag{4}$$

The solid medium thermal conductivity, $\bar{k}_w(T_{io})$, is an average thermal conductivity for the inner wall that is made of stainless steel alloys. It is estimated by the mean value between $k_w(T_{i1})$ and $k_w(T_{4o})$, where $T_{i1} = (T_i + T_1)/2$ and $T_{4o} = (T_4 + T_o)/2$. The reference values were taken from [25]. The convection heat transfer coefficients, for phase i–1, h_{i1}, and phase 4–o, h_{4o}, depend on the average temperature and can be calculated through specific correlations [25] as exposed in Appendix B. Finally, e_w stands for the inner cylinder wall thickness.

2.3.2. Zone 2

The heat transfer in this zone, $\dot{Q}_2$, is modeled as a convective-like heat exchanger, where the air and the inner wall cylinder are involved. The energy balance can be written as:

$$\dot{Q}_2 = \dot{m}\bar{c}_p(T)(T_2 - T_1) + \dot{Q}_{L2} \tag{5}$$

where $\dot{Q}_{L2}$ represents the thermal losses through the insulator (Zone L2, see Fig. 1) and T_1 and T_2 are the air temperatures at Zone 1 and Zone 2, respectively. At the same time, $\dot{Q}_2$ should satisfy:

$$\dot{Q}_2 = h_{wo} A_w \frac{(T_w - T_1) - (T_w - T_2)}{\log \frac{(T_w - T_1)}{(T_w - T_2)}} \tag{6}$$

where h_{wo} is the convective coefficient at the inner cylinder outer surface wall, that depends on temperature as shown in Eq. (B.1). A_w stands for the inner cylinder wall area, but it only comprises the wall area in between the absorbing foam and the glass window. Temperature T_w is the inner wall temperature.

The heat flux, $\dot{Q}_2$, emitted by the wall comes from the absorbing foam and from the glass window. The absorbing foam releases thermal and reflected back visible radiation due to the direct sun beam radiation (I_b) impinging on it. It also receives visible radiation from the glass window. At the same time, the wall losses energy due to the convection with the air crossing Zone 3B, and thermal radiation to the glass window. Then, the following heat balance equation can be considered [27]:

$$\dot{Q}_2 = \overbrace{\tau_g\, I_b\, F_{gf}\cdot \rho_f\, F_{fw}}^{\text{Visible radiation from foam}} + \overbrace{\tau_g\, I_b\, F_{gw}(1 - \rho_w\, F_{wf} - \rho_w\, F_{wg})}^{\text{Visible radiation from glass window}} + \underbrace{\frac{\sigma(T_f^4 - T_w^4)}{\frac{1-\epsilon_f}{A_f\,\epsilon_f} + \frac{1}{A_f\,F_{fw}} + \frac{1-\epsilon_w}{A_w\,\epsilon_w}}}_{\text{Thermal radiation from foam}} - \underbrace{\frac{\sigma(T_w^4 - T_{g,i}^4)}{\frac{1-\epsilon_w}{A_w\,\epsilon_w} + \frac{1}{A_w\,F_{wg}} + \frac{1-\epsilon_g}{A_g\,\epsilon_g}}}_{\text{Thermal radiation to the glass}} - \underbrace{\dot{Q}_{3B}}_{\text{Convection with air}} \tag{7}$$

where ϵ_w, ϵ_f and ϵ_g are the wall, porous foam and glass window emissivities, respectively. Note that the wall is considered a gray body in thermal equilibrium. Thus, the wall absorptivity (*i.e.* the share of energy that the wall will absorb and transfer to the air) is the same as the wall emissivity ($\alpha_w = \epsilon_w$). The share of visible radiation reflected by the foam and by the wall are represented as ρ_f and ρ_w, respectively, while τ_g is the glass window transmissivity. A_f is the cross-sectional foam area, and σ is the Stefan–Boltzmann constant. The term F_{fw} is the view factor between the foam and the wall. It represents the ratio between the amount of thermal radiation leaving the foam that hits the wall [28]. Similarly, F_{wg} is the wall-to-glass view factor, and F_{gf} is the glass-to-foam view factor. The calculus of the view factors is clearly explained in Appendix C. The convective coefficient at the inner cylinder internal surface wall is denoted as $h_{wi}(T)$. Finally, T_f and $T_{g,i}$ are the absorbing foam and the inner glass surface temperatures, respectively. $\dot{Q}_{3B}$ is the convection heat exchange between the inner wall and the fluid, which will be defined later.

2.3.3. Zone 3

Here, the air flows over the internal surface of the glass window. This prevents window breakage since the air flux lowers its temperature. On one hand, there is a convection heat transfer between the air and the inner window surface, which can also be modeled as a heat exchanger. Thus, the following equations can be used:

$$\dot{Q}_3 = \dot{m}\bar{c}_p(T)(T_3 - T_2) \tag{8}$$

$$\dot{Q}_3 = h_{gi} A_g \frac{(T_g - T_3) - (T_g - T_2)}{\log \frac{(T_g - T_3)}{(T_g - T_2)}} \tag{9}$$

where h_{gi} is the convective coefficient at the glass inner surface, A_g is the cross sectional glass area, T_g is the glass window temperature and T_3 and T_2 are the Zone 3 and Zone 2 air temperatures, respectively.

Besides, some other heat transfers occurs at the glass window. It receives visible radiation directly from the Sun (I_b) as well as from the absorber foam ($\sim F_{fg}\,\rho_f\,\tau_g\,I_b$). The window also receives thermal radiation from the wall and the foam. However, it also suffers convection and radiation losses with the ambient. The convection heat transfer with the air can be also considered a 'loss' at the glass window inner surface. All these phenomena can be summarized in the following expression:

$$\overbrace{\alpha_g \cdot I_b + \tau_g\, I_b\,(F_{gf}\,\rho_f\,F_{fg} + F_{gw}\,F_{wg}\,\rho_w)}^{\text{Visible radiation}} + \overbrace{\frac{\sigma(T_f^4 - T_g^4)}{\frac{1-\epsilon_f}{A_f\,\epsilon_f} + \frac{1}{A_f\,F_{fg}} + \frac{1-\epsilon'_g}{A_g\,\epsilon'_g}}}^{\text{Thermal radiation from foam}} + \underbrace{\frac{\sigma(T_w^4 - T_g^4)}{\frac{1-\epsilon_w}{A_w\,\epsilon_w} + \frac{1}{A_w\,F_{wg}} + \frac{1-\epsilon'_g}{A_g\,\epsilon'_g}}}_{\text{Thermal radiation from wall}} = \underbrace{\dot{Q}_3}_{\text{Convection with air}} + \underbrace{h_{go}\,A_g\,(T_g - T_a)}_{\text{Convection with ambient}} + \underbrace{\epsilon'_g\,A_g\,\sigma\,(T_g^4 - T_a^4)}_{\text{Radiation with ambient}} \tag{10}$$

where α_g is the glass absorptance at visible wave. ϵ'_g is the glass emissivity at long wave and F_{fg} is the foam-to-glass view factor. Finally, h_{go} stands for the convective coefficient at the outer glass surface.

2.3.4. Zone 3B

Aiming to model the receiver as realistically as possible, it has been considered a convection heat exchange between the internal wall, on the inner side, with the fluid. This heat transfer is not considered in [14]. The energy balance equations describing this phenomenon will be related to the energy balance at Zone 2 ($\dot{Q}_{3B}$ in Eq. (7)):

$$\dot{Q}_{3B} = \dot{m}\bar{c}_p(T)(T_{3B} - T_3) \tag{11}$$

$$\dot{Q}_{3B} = h_{wi} A_w \frac{(T_w - T_3) - (T_w - T_{3B})}{\log \frac{(T_w - T_3)}{(T_w - T_{3B})}} \tag{12}$$

where h_{wi} is the convective coefficient at the wall inner surface, A_w is the internal wall area, T_w is the wall temperature and T_{3B} and T_3 are the Zone 3B and Zone 3 air temperatures, respectively.

2.3.5. Zone 4

In this stage, the absorbing foam exchanges heat with the air crossing through it. This occurs through convection, so the energy balance equations are:

$$\dot{Q}_4 = \dot{m} \bar{c}_p(T)(T_4 - T_3) \tag{13}$$

$$\dot{Q}_4 = V_f \cdot h_{vf} \frac{(T_f - T_3) - (T_f - T_4)}{\log \frac{(T_f - T_3)}{(T_f - T_4)}} \tag{14}$$

where V_f is the absorber foam vacuum volume $V_f = A_f L_f \phi$. The parameters ϕ and L_f are the foam porosity and foam width, respectively. Zhu et al. [12,14] only provides the pore diameter, d_p, and the Pores Per Inch, (PPI). Thus, the expression from Fu et al. [29] was used for obtaining the absorbing foam porosity: $\phi = (\pi/4)(\mathrm{PPC}\, d_p)^2$, where PPC refers to 'Pores Per Centimeter'. It can be calculated by means of PPI.

The volumetric convective coefficient, h_{vf}, is obtained by following Barreto et al. [30], Wu et al. [31] and Fu et al. [29] works (see Appendix B). Similarly to previous equations, T_4 stands for the air temperature at the foam outlet. Besides, an energy balance for the absorber foam system must be established. The foam absorbs the visible radiation coming from the glass window, but it also suffers some losses: visible radiation reflected, convection heat transfer with the air, and thermal radiation emitted to the wall and glass. So, the following equation can be written:

$$\overbrace{\tau_g I_b F_{gf}(1-\rho_f)}^{\text{Visible from glass to foam}} + \overbrace{\tau_g I_b F_{gw} \cdot F_{wf} \rho_w}^{\text{Visible from wall to foam}} = \dot{Q}_4 + \underbrace{\frac{\sigma(T_f^4 - T_w^4)}{\frac{1-\epsilon_f}{A_f \epsilon_f} + \frac{1}{A_f F_{fw}} + \frac{1-\epsilon_w}{A_w \epsilon_w}}}_{\text{Thermal radiation to the wall}} + \underbrace{\frac{\sigma(T_f^4 - T_g^4)}{\frac{1-\epsilon_f}{A_f \epsilon_f} + \frac{1}{A_f F_{fg}} + \frac{1-\epsilon_g}{A_g \epsilon_g}}}_{\text{Thermal radiation to the glass}} \tag{15}$$

2.3.6. Heat losses at the insulator: Zone L1

This zone refers to the cylindrical insulator from the inlet pipes until the absorber foam plane. It also considers the plane surface surrounding the inlet and outlet pipes, as depicted in Fig. 1. The heat transfer across the insulator surfaces will be modeled as a heat exchanger (LMTD expression will be considered). So, the heat transferred from the air to the insulator (convection and conduction) must be the same as the heat flux from the outer insulator surface to the surroundings (convection and radiation).

$$\dot{Q}_{L1} = A_{iL1} U_{L1} \frac{(T_1 - T_{L1}) - (T_i - T_{L1})}{\log \frac{(T_1 - T_{L1})}{(T_i - T_{L1})}} \tag{16}$$

where $\dot{Q}_{L1}$ denotes the heat flux that is lost through the Zone L1. A_{iL1} stands for the internal insulator area, including the cylindrical and circular surfaces. U_{L1} is a global heat transfer coefficient, which accounts for the cylindrical and plane zones. Thus, $A_{iL1} U_{L1}$ can be written as:

$$A_{iL1} U_{L1} = A_{iL1.cyl} U_{cyl.L1} + A_{iL1.flat} U_{flat.L1} \tag{17}$$

where [25]:

$$A_{iL1.cyl} = 2\pi r_i L_1 \tag{18}$$

$$U_{cyl.L1} = \left[\frac{1}{h_{L1,in}} + \frac{r_i \log(r_o/r_i)}{\bar{k}_i(T_{1,i,L1})} \right]^{-1} \tag{19}$$

$$A_{iL1.flat} = \pi (r_i^2 - r_{p,o}^2 - 3 r_{p,i}^2) \tag{20}$$

$$U_{flat.L1} = \left[\frac{1}{h_{L1,in}} + \frac{e_o}{\bar{k}_i(T_{1,i,L1})} \right]^{-1} \tag{21}$$

Within expressions (19) and (21), $h_{L1,in}$ represents an average convection coefficient for the inner insulator cylindrical and circular surfaces, both of them approximated for 'convection over a flat plate' (see Appendix B). The radius r_i denotes the inner insulator cylinder radius while r_o accounts for the external insulator radius. Note that $r_i = r_f + e_w + e_i$ and $r_o = r_i + e_o$ (see Fig. 1(b)). $\bar{k}_i(T_{1,i,L1})$ stands for the insulator average conduction coefficient between temperatures T_i, T_1 and T_{L1}. $r_{p,i}$ and $r_{p,o}$ are the inlet and outlet pipes radius. The effective flat area, $A_{iL1.flat}$, does not include the three inlet pipes nor the outlet pipe (see Eq. (20)). Finally, e_o is the insulator thickness. The last heat exchange occurs at the outer insulator surface, where convection and radiation with the surroundings has been considered. Thus, these phenomena can be described through the following expression [27]:

$$\dot{Q}_{L1} = A_{o1} \left(h_{c,L1} + h_{r,L1} \right) (T_{L1} - T_a) \tag{22}$$

where A_{o1} represents the insulator outer surface area in Zone L1, including cylindrical and flat ones:

$$A_{o1} = A_{o1,cyl} + A_{o1,flat} = 2\pi r_o L_1 + \pi (r_o^2 - r_{p,o}^2 - 3 r_{p,i}^2) \tag{23}$$

In this equation, $h_{c,L1}$ is the convection coefficient between the outer insulator surface temperature (T_{L1}) and ambient temperature (T_a), while $h_{r,L1}$ stands for the radiation coefficient under the same conditions. This radiation coefficient can be written as follows [27]:

$$h_{r,L1} = \epsilon_{L1} \sigma (T_{L1} + T_a)(T_{L1}^2 + T_a^2) \tag{24}$$

where ϵ_{L1} is the outer insulator surface emissivity.

2.3.7. Heat losses at the insulator: Zone L2

This zone refers to the cylindrical insulator from the absorber foam plane until the glass window plane. It also takes into account the plane surface surrounding the glass window, as depicted in Fig. 1. Similarly to Zone L1, the heat transfer across the insulator surfaces will be considered as heat exchangers.

$$\dot{Q}_{L2} = A_{iL2} U_{L2} \frac{(T_2 - T_{L2}) - (T_1 - T_{L2})}{\log \frac{(T_2 - T_{L2})}{(T_1 - T_{L2})}} \tag{25}$$

where $\dot{Q}_{L2}$ denotes the heat flux lost through the insulator front side. $A_{iL2} U_{L2}$ is a global heat transfer coefficient, which accounts for the cylindrical and plane zones. Thus, $A_{iL2} U_{L2}$ can be written as:

$$A_{iL2} \cdot U_{L2} = A_{iL2.cyl} U_{cyl.L2} + A_{iL2.flat} U_{flat.L2} \tag{26}$$

where:

$$A_{iL2.cyl} = 2\pi r_i L_2 \tag{27}$$

$$U_{cyl.L2} = \left[\frac{1}{h_{L2}} + \frac{r_i \log(r_o/r_i)}{\bar{k}_i(T_{2,1,L2})} \right]^{-1} \tag{28}$$

$$A_{iL2.flat} = \pi (r_i^2 - r_g^2) \tag{29}$$

$$U_{flat.L2} = \left[\frac{1}{h_{L2}} + \frac{e_o}{\bar{k}_i(T_{2,1,L2})} \right]^{-1} \tag{30}$$

The coefficients are analogous to those explained for Eqs. (19) and (21). The only difference is that, here, the temperatures involved are T_2, T_1 and T_{L2} (the outer insulator surface temperature in Zone L2) as depicted in Fig. 1. r_g stands for the receiver glass window radius.

Again, the heat released from the outer insulator surface to the surroundings, can be described by:

$$\dot{Q}_{L2} = A_{o2}\left[h_{c,L2} + h_{r,L_2}\right](T_{L2} - T_a) \tag{31}$$

where A_{o2} represents the insulator outer surface area within Zone L2, including cylindrical and flat ones:

$$A_{o2} = A_{o2,cyl} + A_{o2,flat} = 2\pi r_o L_2 + \pi(r_o^2 - r_g^2) \tag{32}$$

and $h_{c,L2}$ is the convection coefficient between the outer insulator surface temperature (T_{L2}) and ambient temperature (T_a), while $h_{r,L2}$ stands for the radiation coefficient under the same conditions, which has been established as [27]:

$$h_{r,L2} = \epsilon_{L2}\sigma(T_{L2} + T_a)(T_{L2}^2 + T_a^2) \tag{33}$$

where ϵ_{L2} is the outer insulator surface emissivity.

2.3.8. Receiver thermal energy efficiency

All previous equations allow for calculating the receiver efficiency, $\eta_{th,rcv}$, by means of Eq. (1). However, the efficiency can also be expressed as a function of heat losses as follows:

$$\eta_{th,rcv} = 1 - \frac{\dot{Q}_g + \dot{Q}_{L1} + \dot{Q}_{L2} + \rho_g I_b}{I_b} \tag{34}$$

where $\dot{Q}_g$ stands for the conductive and convective losses from the glass to the ambient and the term $\rho_g I_b$ accounts for the solar energy reflected back by the glass window.

3. Validation

In this section, the validation of the Tonatiuh optical model and solar receiver numerical model are presented.

3.1. Tonatiuh software

Two steps are needed for obtaining the parabolic dish optical efficiency, η_{opt}, through Tonatiuh software: Monte-carlo ray tracing within the Tonatiuh environment and post-processing of the output files. Tonatiuh itself has already been validated in other works [24,32]. Thus, the validation will be focused on the Mathematica® post-processing program, which was modified from the Ref. [33].

Two setups were analyzed for carrying out the validation. On one hand, Barreto and Canhoto's model [2] was chosen because of the completeness of the information provided for performing Tonatiuh simulations. On the other hand, the solar receiver model exposed in Section 2 was designed for Zhu's dish prototype [12], so validation was also done against their results.

Barreto and Canhoto's work [2] presents a comparison of the optical efficiencies of several dishes with different concentration factors (CF). They provide a detailed description of the parameters selected. Those are exposed in Table 2. During this analysis, the influence of the number of rays in the predicted efficiencies was checked. It was shown that from 1 million rays, the efficiency does not significantly vary. Thus, the simulations carried out with 25 million rays are considered as precise enough (see Appendix D).

The optical efficiency considers not only a flat disk at the receiver, but also a surrounding cylinder. This is due to the fact that a Stirling engine is linked to the PDC that Barreto and Canhoto simulate. Therefore, the thermal receiver is directly one of the pistons compounding the power block. The receiver is then composed of a flat surface disk placed at the basis of a cylinder and the cylinder itself. The expression for the overall optical efficiency in this case is [2]:

$$\eta_{opt} = \frac{P_{cir} + P_{cyl}}{P_{dis}} \tag{35}$$

where P_{cir} is the incident power at the circular basis disk, P_{cyl} is the power impinging at the cylinder surface and P_{dis} is the incident solar power at the aperture area of the PDC. While P_{dis} depends on the DNI and the aperture area, P_{cir} and P_{cyl} are calculated by numerically integrating the incident radiation flux arriving at each surface [2]. The results obtained after performing the simulations are exposed and compared in Table 3.

Table 2
Tonatiuh optical parameters for the validation with Barreto and Canhoto's work [2].

Parameter	Value			
DNI (W/m^2)	800			
Sun shape	Buie distribution			
CSR	2%			
Number of rays	$25 \cdot 10^6$			
Collector				
ρ_d (–)	0.95			
σ_s (mrad)	0			
CF	100	200	250	400
A_{ap}(cm^2)	0.507	1.005	1.255	2.003
D (cm)	0.803	1.131	1.263	1.597
ψ (°)	32.01	44.00	48.59	59.39
f_d (cm)	70			
Receiver (Cylinder & Disk flat basis)				
r_{cyl} (cm)	1.8			
H_{clmax} (cm)	3.41			
r_{cir} (cm)	1.8			

The relative difference for the overall optical efficiency, η_{opt}, does not overcome 0.05% at any configuration. There exists a systematic difference at the power arriving at the circular flat basis, P_{cir}, and at the cylindrical surface, P_{cyl}. However, for all the cases, those differences do not overpass 4.4% in relative terms.

As previously mentioned, a validation process is also performed for Zhu's PDC prototype [12]. The PDC modeled here, takes a particular geometry (from Zhu's work, see Fig. 3) for numerical computations. In Table 4, the parameters used for the simulation with Tonatiuh are shown.

The Tonatiuh flat disk placed at the focus can represent either the receiver's window (for volumetric receivers) or the cross sectional area of a cavity (for cavity receivers). Besides the flat disk, other geometries can be configured for receivers simulations. In this case, the receiver glass window will be approached as a flat disk.

The overall solar efficiency for the set-up analyzed here is the ratio between the total power impinging at the receiver flat disk (glass window), P_{rcv}, and the amount of radiation flux collected by the PDC, P_{dis}:

$$\eta_{opt} = \frac{P_{rcv}}{P_{dis}} \tag{36}$$

The relative difference obtained for the optical efficiency is less than 0.15% (see Table 5). The optical efficiency value provided by Zhu's work comes from experimental data measurements. Thus, it seems coherent to obtain a higher relative difference in the optical efficiency when compared with Barreto and Canhoto. Therefore, validation results are satisfactory.

3.2. Solar receiver

In this subsection, the validation for the solar receiver model is presented. Here, the optical efficiency is considered the same as the one provided by Zhu et al. ($\eta_{opt} = 0.8645$ [12], see Table 5). In Table 6, the values of all parameters required to numerical computations are enclosed. A compressor pressurizes the air at a pressure around 5 times the atmospheric pressure [14] before entering the receiver.

In Fig. 4, a comparison between the values obtained in this work and Zhu et al. [14] results is depicted. It shows a good agreement, especially in the medium zone of the temperature interval. The smallest

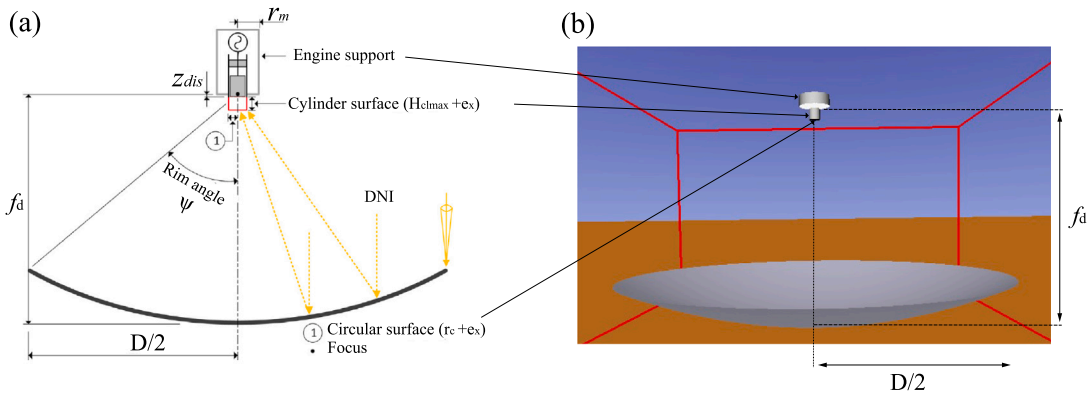

Fig. 2. Scheme of PDC used for this work: (a) Barreto et al. configuration, (b) Replication of Barreto's model on Tonatiuh. *Source:* Adapted from Barreto et al. [2].

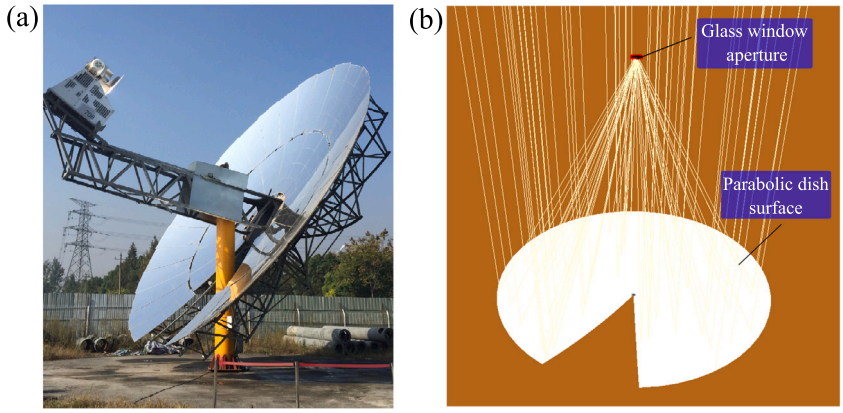

Fig. 3. Scheme of PDC used for this work: (a) Zhu et al. real prototype and (b) replication of Zhu's prototype on Tonatiuh. *Source:* Adapted from Zhu et al. [12].

Table 3
Validation of Tonatiuh simulations against the results from Barreto and Canhoto [2]. The column at the right represents the relative differences in percentage.

CF		P_{dish} (W)	P_{cir} (W)	P_{cyl} (W)	η_{opt} (%)	η_{opt} relative difference (%)
100	Ref. [2]	398.97	185.74	191.59	94.60	0.03
	This work	399.18	177.90	199.82	94.62	
200	Ref. [2]	797.32	186.27	567.99	94.60	0.05
	This work	797.89	178.27	576.20	94.56	
250	Ref. [2]	997.32	186.42	756.05	94.50	0.01
	This work	997.82	178.39	764.83	94.49	
400	Ref. [2]	1596.13	186.73	1286.50	92.30	0.03
	This work	1595.55	178.57	1294.54	92.33	

relative difference (0.05%) is found at 861.8 K. The greater relative differences are found at the lowest temperature (1.06% at 523.9 K) and at the highest temperature (0.83% at 953.3 K). The relative difference is below 1.5% for all the cases. Thus, it can be considered that the model presented here has been validated.

4. Results: Cases of study

The model presented here can be used to predict the thermal receiver efficiency, the fluid temperatures across the receiver zones, and the receiver surfaces temperatures. All of them can be computed for specific locations with different meteorological conditions. For each pair of DNI and ambient temperature (T_a) values, the system of equations is solved under steady-state conditions with constant mass flow assumed to operate at on-design conditions. Additional assumptions are steady conditions for each point in hourly evolution curves, a constant inlet pressure of the working fluid, a global pressure decay along the whole receiver, and an effective temperature for the absorber (position independent).

The optical parameters for the dish are taken in all cases as in Table 4 (except DNI that will be a time-dependent parameter) and the parameters for the glass window, inner cylinder wall, foam, receiver geometry, and view factors as in Table 6.

4.1. Fluid and surfaces temperatures at the receiver

The location selected is Ouarzazate (Morocco) and the days analyzed are one day in summer (June 24th, 2021) and one day in winter (December 22nd, 2021), on purpose selected because of its poor solar

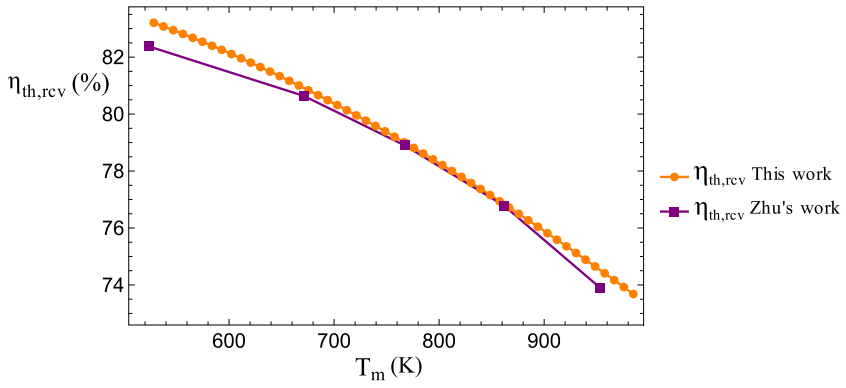

Fig. 4. Solar receiver thermal efficiency as a function of mean receiver temperature, T_m: Comparison between Zhu's model (purple) and this work (orange).

Table 4
Tonatiuh optical parameters for the validation against Zhu's work [12].

Parameter	Value
DNI (W/m^2)	600
Sun shape	Buie distribution
CSR	2%
Sun position	0° (azimuth)
	90° (elevation)
Number of rays	$25 \cdot 10^6$
Collector	
ρ_d (–)	0.87
σ_s (mrad)	0.5
CF	1750
A_{ap}(m^2)	44
D (m)	3.74
ψ (°)	45
f_d (m)	6.7
Receiver (Glass window flat disk)	
r_g (m)	0.125

Table 5
Validation of Tonatiuh post-processing program with the results provided by Zhu [12].

	P_{dish} (kW)	P_{rcv} (kW)	η_{opt} (%)	η_{opt} relative difference (%)
Ref. [14]	–	–	86.45	0.12
This work	23.72	20.48	86.35	

conditions. Ouarzazate (30.92° N latitude) already has CSP technologies installed (NOOR I and NOOR II [34]), so it is considered a suitable location for CSP installations because of its large solar resources. Annual direct normal irradiation is over 2500 kWh/m^2. Mean minimum temperature is around 282 K (9 °C) and maximum around 294 K (21 °C, approximately) [35]. Meteorological data were taken from MERRA (Modern-Era Retrospective Analysis) for the ambient temperature and from Copernicus Europe's eyes on earth for the DNI data. Both of them were provided by Solar Radiation Data (SoDa) Service [36,37].

In Fig. 5(a), fluid temperatures throughout the receiver are represented during the summer day. The inlet temperature, T_i, and temperature T_1 are always about 200 K above ambient temperature, T_a, because the compressor pressurizes the air going to the receiver. Temperatures T_2, T_3 and T_{3B} achieve a maximum of about 700–715 K. T_4 and T_o achieve temperatures above 1200 K. While T_i and T_1 seem to follow ambient temperature behavior, temperatures T_2, T_3, T_{3B}, T_4 and T_o behave like DNI curve (see Fig. 7(a) below).

In Fig. 5(b) the same temperatures are depicted for the winter day with poor solar conditions. Temperature profiles are different from the summer day because of the lower DNI and ambient temperature. However, the relations between the temperatures are similar, *i.e.*, T_i and T_1 keep following ambient temperature behavior, while temperatures T_2, T_3, T_{3B}, T_4 and T_o have a shape similar to DNI curve. For those DNI values higher than 35 W/m^2, the inlet temperature, T_i, and temperature T_1 are also about 200 K above ambient temperature, T_a. T_i and T_1 barely reach 490 K. However, the rest of the temperatures (T_2, T_3, T_{3B}, T_4 and T_o) are clearly and directly influenced by DNI levels. Here, T_2, T_3 and T_{3B} do not overpass 519 K, and T_4 and T_o achieve maximum values of 664 K and 662 K, respectively.

In Figs. 5(c) and (d), fluid temperatures are represented for a specific time within the day. Noontime (12:00 PM) was selected for June 24th (Fig. 5(c)). At this point, the DNI achieves its maximum value (950 W/m^2, see Fig. 7(a) below). In Fig. 5(c) it is depicted how the air rises its temperature from 528.7 K (T_i, temperature at the outlet of the compressor) up to 1196.42 K (T_4, the temperature after crossing the porous foam). The outlet temperature (T_o) is approximately 12.3 K below T_4, due to the heat exchange between the receiver outlet and inlet (Zone 1). Here, there is a temperature increase of about 654 K. In December (Fig. 5(d)), the temperature profile in winter is almost flat, since the temperatures across the different receiver's zones do not strongly change. In particular, the fluid temperature difference between T_o (662.02 K) and T_i (493.88 K) is only 168 K, approximately.

Finally, in Figs. 5(e) and (f), receiver surfaces temperatures were depicted for the same time (noon and 14:30 PM, respectively). The highest temperature among the surfaces is achieved at the porous foam, T_f, (1245.2 K, in June, Fig. 5(e)). There is a difference of 378 K between the inner and outer glass surfaces ($T_{g,i}$ and $T_{g,o}$, respectively). This temperature difference is proportional to the heat losses across the glass window ($\dot{Q}_g$). The insulator surface temperatures for Zone L1 (T_{L1}=376.66 K) and Zone L2 (T_{L2}=354.45 K), are about 70 K above ambient temperature. The wall surface temperature (T_w=1089.04 K) is close to the inner glass window surface temperature, but it never overcomes it. Although the temperatures are about 200–500 K lower in December (Fig. 5(f)), the surface temperature profile is the same.

4.2. Heat transfers in the receiver

In Fig. 6 the considered heat transfers within the model are depicted for the same two days, as a function of daytime (Figs. 6(a) and (b)) and for two fixed hours (Figs. 6(c) and (d)). It is clear that the heat absorbed inside the porous foam, $\dot{Q}_4$ (red), is the highest heat flux contribution to the fluid for raising its temperature, followed by $\dot{Q}_2$ (yellow). At the same time, the heat losses through the glass window, $\dot{Q}_g$ (magenta), account for one of the main losses within the receiver. Finally, the most important losses are $\rho_g I_b$, *i.e.*, the share of visible radiation that is reflected back at the time of hitting the glass window.

4.3. Optical and thermal efficiencies for different locations and conditions

The optical (gray) and thermal receiver (green) efficiencies are depicted in Fig. 7 at specific locations under different meteorological

Table 6
Solar receiver parameters for the validation with Zhu's [14] work.

Parameter	Value (unit)	
DNI	600 W/m^2	Solar heat flux impinging at the glass window
σ	5.67 10^{-8} W/(m^2 K^4)	Stefan–Boltzmann constant
$\dot{m}$	0.04 kg/s	Mass flow rate
η_{opt}	0.8645	Dish optical efficiency
A_d	44 m^2	Dish aperture area
Glass window		
ρ_g	0.136	Reflectivity at visible wave
τ_g	0.851	Transmissivity at visible wave
α_g	0.013	Absorptivity at visible wave
α'_g	1	Absorptivity at long wave (perfect)
r_g	0.125 m	Radius
L_g	0.015 m	Glass thickness
Inner cylinder wall		
ρ_w	0.2	Reflectivity at visible wave
ϵ_w	0.8	Emissivity (gray body at thermal equilibrium)
A_w	0.1788 m^2	Total area share of wall placed between porous matrix and
e_w	0.001 m	Wall thickness
Foam porous matrix		
ρ_f	0.05	Reflectivity at visible wave
ϵ_f	0.95	Emissivity (gray body at thermal equilibrium)
r_f	0.182 m	Radius
L_f	0.065 m	Foam width
ϕ	0.792 (–)	Porosity
PPI/PPC	75/29.53	Pores Per Inch/ Pores Per Centimeter
d_p	$3.40{\cdot}10^{-4}$ m	Pore diameter
d_c	$1.86{\cdot}10^{-3}$ m	Average pore cell diameter
l_s	$6.58{\cdot}10^{-4}$ m	Strut length
d_s	$3.68{\cdot}10^{-4}$ m	Strut diameter
Geometrical parameters		
L_1	0.195 m	Receiver length for the phase i – 1 (to the right of the foam)
L_2	0.1079 m	Receiver length for the phase 1 – 2 (to the left of the foam)
e_i	0.014 m	Radius difference between inner wall and insulator cylinders
r_i	0.136 m	Internal insulator radius
e_o	0.003 m	Insulator thickness
r_o	0.2 m	External insulator radius
Inlet and outlet pipes		
$r_{p,i}$	0.01 m	Inlet pipe radius
$r_{p,o}$	0.042 m	Outlet pipe radius
View factors		
F_{fg}	0.2956	Foam porous matrix to glass window
F_{fw}	0.7044	Foam porous matrix to inner wall
F_{gf}	0.6267	Glass window to foam porous matrix
F_{gw}	0.3733	Glass window to inner wall
F_{wf}	0.4110	Inner wall to foam porous matrix
F_{wg}	0.1027	Inner wall to glass window

conditions. Besides Ouarzazate (Morocco), Salamanca (Spain) was also selected for performing the simulations. Salamanca (40.96°N latitude) is located on a plateau at about 800 m above sea level. It has a dry continental climate. Summers are dry and hot and winters cold with not much rain. The annual insolation is about 1834 kWh m^{-2} y^{-1}. During winter months, the daily average temperatures could be around 278 K (from December to March). The annual mean temperature in Salamanca is 285 K (12° C) [38]. The mass flow rate remains constant in these simulations. Apart form satellite data, *in situ* DNI and ambient temperature data recorded at the University of Salamanca were considered (Fig. 7(c), (f) and (i)). One additional objective of the work is to compare possible differences between satellite DNI data and in situ measures even at a relatively good location, although always subject to local meteorological conditions or surroundings shadows. The equipment for measures includes two pyranometers Kipp and Zonen SMP10, Class A and a shadow ring CM121 B/C [39] and a meteorological station Lufft WS10 [40].

For both locations, three representative days of the different seasons were selected: one day in summer (June 24th, 2021), one day in spring (March 24th, 2021) and one day in winter (December 22nd, 2021). The variation of DNI (orange) and ambient temperature (T_a, cyan) are also attached. The optical efficiency, η_{opt}, values obtained with Tonatiuh software follow a step function shape for all the locations and seasons. Optical efficiency is computed for DNI values over 2 W/m^2. Values are in the range from 86.27% to 86.57% among the locations and days considered. This means a relative difference of 0.35% among locations and seasons.

The receiver thermal efficiency, $\eta_{th,rcv}$, is about 6% below the optical one, η_{opt}, for the hours in which DNI values have no oscillations (specially June and March). Under these conditions, $\eta_{th,rcv}$ looks like a plateau. Values of the receiver thermal efficiency, $\eta_{th,rcv}$, achieved in June (Fig. 7(a), (b) and (c)) are 80.32% at Ouarzazate, 80.52% at Salamanca and 80.61% for the *in situ* data recorded at Salamanca. Ambient temperatures are lower in March, but the good levels of DNI yield to similar values for $\eta_{th,rcv}$ (Fig. 7(d), (e) and (f)). The maximum $\eta_{th,rcv}$ values are: 80.56% at Ouarzazate, 80.61% for Salamanca, and 80.75% for the *in situ* data recorded at Salamanca.

In December, $\eta_{th,rcv}$ sudden variations are due to the DNI abrupt oscillations (Fig. 7(g), (h) and (i)). It is noticeable that, in Fig. 7(g), there are a few peaks regarding the optical efficiency, η_{opt}. However, the thermal efficiency, $\eta_{th,rcv}$, has only 3 peaks. This is caused by the fact that Tonatiuh DNI threshold is 2 W/m^2, while thermal receiver model equations need at least 35 W/m^2 for the equations to converge. Nevertheless, if DNI overcome the minimum for the equations to converge, $\eta_{th,rcv}$ achieves maximum values of 78.14% (Ouarzazate), 80.59% (Salamanca) and 80.60% (Salamanca *in situ* data).

In regards to all previous results, it must be noticed that, if DNI does not overcome the minimum value of 35 W/m^2 (necessary for the

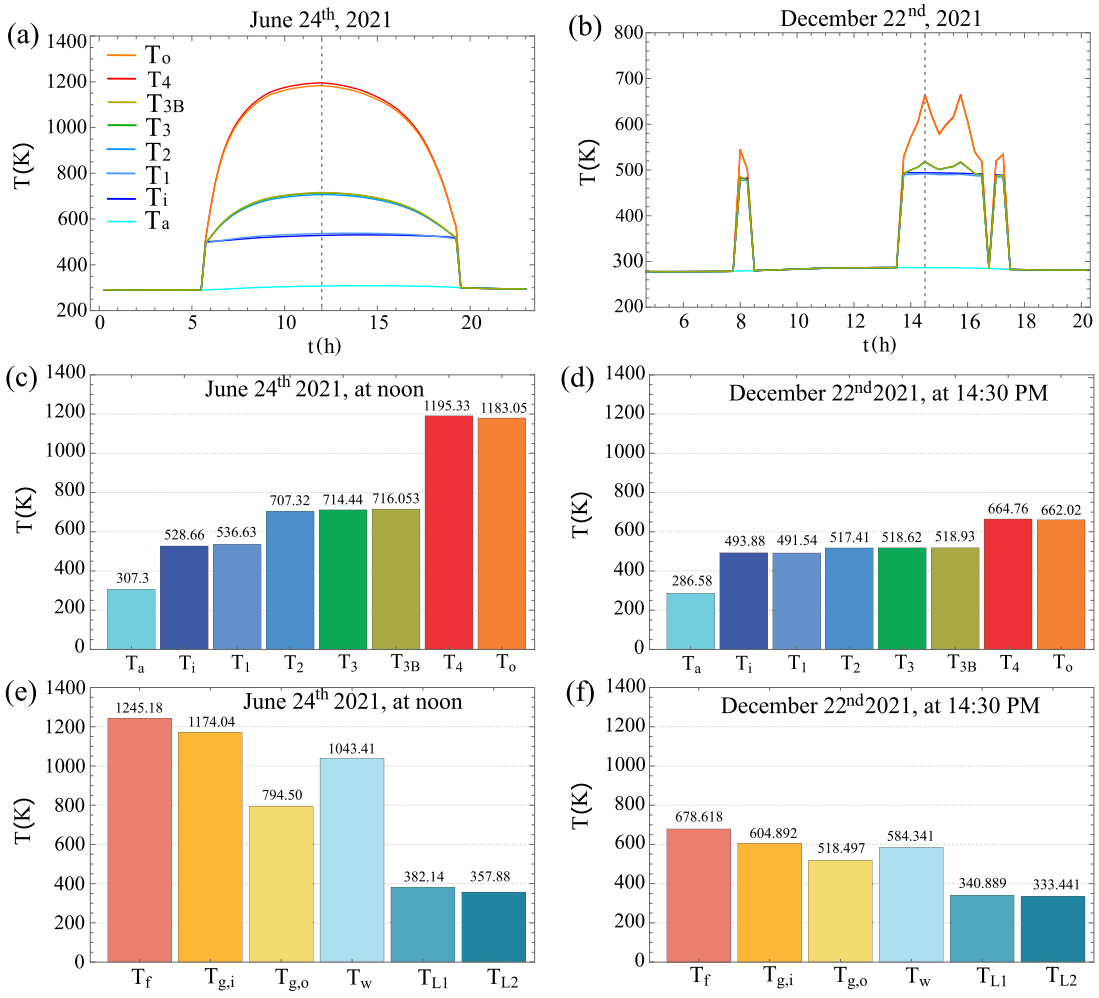

Fig. 5. Fluid temperatures during its flow through the receiver and material temperatures at Ouarzazate (Morocco): (a),(b) Fluid temperatures throughout the considered days (note that scales are different); (c),(d) fluid temperatures and (e),(f) receiver surfaces temperatures at particular times. Time is expressed in UTC (Universal Time Coordinated). The times selected for (c) and (d) charts are indicated with a gray dashed vertical line in (a) and (b) plots, respectively.

set of equations to converge), the system is switched off. Under those circumstances, the compressor is not working, and all the temperatures are equal to the ambient temperature. Once the minimum DNI is overcome, the compressor is supposed to start working instantly, since no transitory behavior was considered within this model. Another limitation within the model is the calculus of the pressure drop. Although an effective pressure drop was considered, a more realistic approach could be carried out. There could be a significant pressure drop along the receiver, especially inside the porous absorber. This feature was considered by Hassan et al. [41] using an analytical equation for calculating the pressure drop after crossing a porous material, which takes into account the fluid density, superficial velocity, porosity and Reynolds number.

5. Summary and conclusions

A physical model to study the thermal performance of a pressurized solar receiver associated with a parabolic dish, small-scale, CSP system was presented. The ray tracing software Tonatiuh [3] was used for obtaining the parabolic dish optical efficiency. All the schemes, hypotheses, and equations describing the receiver model and the calculation of its thermal efficiency were presented in detail. This model can be applied to different receiver geometries and materials at stationary conditions. Particularly, quartz glass on the window and a metallic foam in the absorber were considered. All the main heat transfer efficiencies were modeled and computed, allowing for a precise estimation of receiver thermal efficiency without paying excessive computational effort. Improvements with respect to previous models include: volumetric heat transfer coefficient for the receiver foam, distinct temperatures inside and outside the glass window, heat losses through the insulator, accurate expressions for thermal radiation exchanges, and a precise set of view factors.

Both submodels, for calculating the optical efficiency of the collector and thermal efficiency of the receiver, were validated against previous results in the literature. Discrepancies in the case of the optical efficiency are always below 0.12% and for the thermal efficiency of the receiver below 1.5%, so models hypotheses appear to be robust.

Different cases of study were presented and analyzed, including two locations with different meteorological conditions: Ouarzazate (Morocco) and Salamanca (Spain), and three seasons (spring, summer and winter). Thus, the physical mechanisms influencing receiver efficiency were estimated under real conditions in daily basis. This allows for calculating, for any value of DNI and ambient temperature, the temperatures of the heat transfer fluid and receiver surfaces at any stage. Besides, it has been shown that this model is capable to quantify heat transfer flows and losses to the ambient in each zone of the receiver. The largest heat transfer is produced at the metallic foam and the main losses are associated with the reflectivity of the external wall of the glass.

From the presented results, it could be concluded that, under the operation strategy followed in this work (mass flow remain constant),

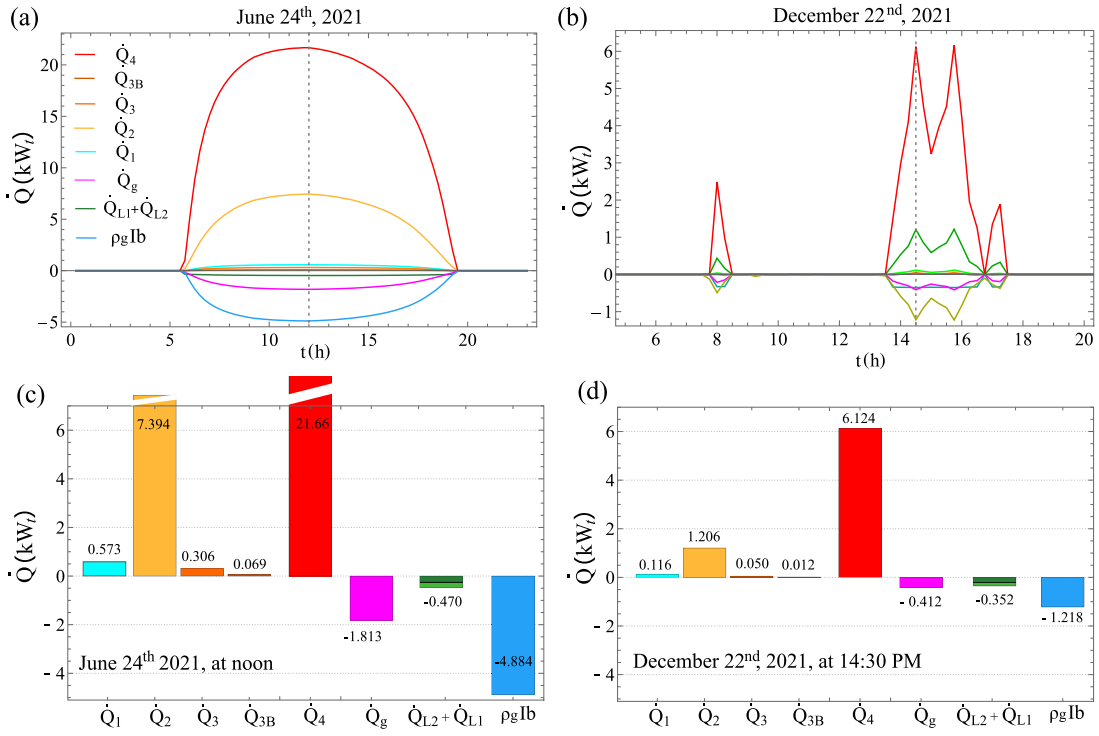

Fig. 6. Heat transfers ($\dot{Q}_1$, $\dot{Q}_2$, $\dot{Q}_3$, $\dot{Q}_{3B}$ and $\dot{Q}_4$) and losses ($\dot{Q}_g$, $\dot{Q}_{L1}$, $\dot{Q}_{L2}$ and $\rho_g I_b$) along the receiver at Ouarzazate (Morocco): (a),(b) as functions of time (x, y-axes scales are different) and (c),(d) for fixed hours.

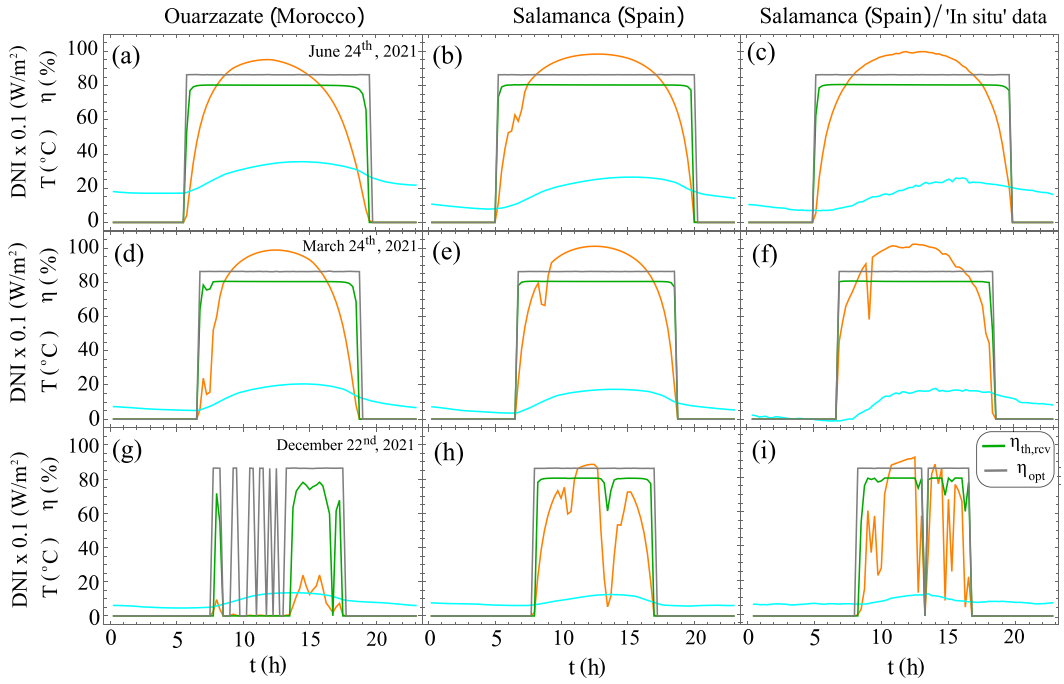

Fig. 7. Solar receiver thermal efficiency (green) and optical efficiency (gray) for two locations (Ouarzazate and Salamanca) along three representative days of 2021 for different seasons: summer, spring and winter. DNI (orange) is scaled by 0.1 factor and represented in W/m^2, ambient temperature (cyan) is represented in °C, and optical and receiver thermal efficiencies are plotted in %. (a), (b) and (c) figures represent the summer season for Ouarzazate, Salamanca (satellite), and Salamanca *in situ* data (d), (e) and (f) figures represent the spring season. (g), (h) and (i) figures represent the winter season for the same locations.

receiver thermal efficiency is strongly influenced by DNI daily curves. The inlet temperature and also the enthalpy at the inlet directly depend on the ambient temperature curve. However, they have little or almost negligible influence over $\eta_{th,rcv}$ results.

All results obtained for the considered cases of study were obtained assuming a constant mass flow of air, quasi-steady conditions for each point in hourly evolution curves, a constant inlet pressure of the working fluid, a global pressure decay along the whole receiver, and an effective temperature for the absorber (position independent). These *thermodynamic-based* models allow a comprehensive description of each involved subsystem with a non too much complex set of equations from which some physical parameters with a clear interpretation emerge. These features could allow the implementation of sensitivity analysis, and optimization techniques. Anyway, these methodological limitations could be avoided with different (computationally expensive) approaches, as computational fluid dynamics simulations that, nevertheless, would make less straightforward the calculation of the integrated optical/receiver efficiency and its evolution with real meteorological and solar conditions.

As future development, the solar receiver model is planned to be coupled with thermodynamic models for the power unit associated, as Brayton or other cycles, in order to produce distributed electric power. Thus, it would be possible to analyze the behavior of the whole CSP plant and to suggest improvements for design or operation with enough precision and without applying techniques requiring a huge computational effort.

CRediT authorship contribution statement

J. García Ferrero: Methodology, Software, Validation, Writing – original draft, Writing – review & editing. **R.P. Merchán:** Writing – review & editing. **M.J. Santos:** Conceptualization, Methodology, Writing – review & editing, Supervision. **A. Medina:** Conceptualization, Methodology, Writing – original draft, Writing – review & editing, Supervision. **A. Calvo Hernández:** Funding acquisition, Supervision, Writing – review & editing. **P. Canhoto:** Conceptualization, Formal analysis. **A. Giostri:** Software, Writing – review & editing.

Declaration of competing interest

The authors declare that they have no known competing financial interests or personal relationships that could have appeared to influence the work reported in this paper.

Data availability

Data will be made available on request.

Acknowledgments

Financial support from Institute of Fundamental Physics and Mathematics (IUFFYM) and Escuela de Doctorado 'Studii Salamantini' from University of Salamanca is acknowledged. European Union, 'Next Generation EU' financial support, within 'Programa Investigo, Plan de Recuperación, Transformación y Resiliencia', Junta de Castilla y León and Universidad de Salamanca, is also acknowledged. SoDa Transvalor/MINES ParisTech is acknowledged for the meteorological and solar radiation data provided.

Appendix A. Polynomial expressions for specific heats, thermal conductivity and viscosity.

Aiming to reduce the computational time, in each heat transfer process, a polynomial expression for the mean isobaric thermal capacity, $\bar{c}_p$, was obtained by averaging an interpolation polynomial between the coldest temperature, T_c, and the hottest one, T_h:

$$\bar{c}_p = \frac{1}{T_h - T_c} \int_{T_c}^{T_h} \left(a + b\,T + c\,T^2 + d\,T^3 + e\,T^4 + f\,T^5\right)\,dT \tag{A.1}$$

where the coefficients a, b, c, d, e and f for dry air are shown in Table A.7.

Eq. (A.1) is employed within the energy balance equations in the receiver's model. The air thermal conductivity, $k_{air}(T_m)$ and air dynamic viscosity, $\mu(T_m)$, were calculated by means of Mathematica®software, as well as it was done with $c_p(T)$. The coefficients for the polynomial expression obtained for the air thermal conductivity in the range of 200 to 1500 K are shown in Table A.7, along with the coefficients for the dynamic viscosity, $\mu(T_m)$.

Appendix B. Convection heat transfer coefficients (h)

This section explains how the heat transfer coefficients have been calculated for each zone in the receiver and the main assumptions considered. For all the cases, the receiver is considered at horizontal position. Except for the outer glass window surface, all the other receiver zones will be considered under forced convection. The convection heat transfer coefficients, h, can be calculated through the Nusselt number expression as follows [25]:

$$Nu_{L_C}(Re, Pr) = \frac{h}{k_{air}(T_m)/L_C} \longrightarrow h = \frac{Nu_{L_C}(Re, Pr) \cdot k_{air}(T_m)}{L_C} \tag{B.1}$$

where L_C stands for a characteristic length. Re and Pr are the Reynolds and Prandtl numbers, respectively.

B.1. Zone 1

As previously explained in Eq. (4), the heat transfer at this stage is assumed to behave like a heat exchanger. There is not a defined temperature at the cylinder inner wall but a constant heat flux $\dot{Q}_1$ will be considered.

The Nusselt number contemplated at the receiver entry (phase i – 1) is the one obtained by Gnielinski Formula [14,25] (forced convection and turbulent flow). For the laminar regime, it will be treated as two parallel plates [25] because the difference between the inner and the outer diameter is negligible compared to the tubes diameter. Thus, the Nusselt number for the heat transfer at the entry region is:

$$Nu_{i1} = Nu_{D_h}(Re, Pr) = \begin{cases} \dfrac{(f_P/8)\cdot(Re-1000)\cdot Pr}{1+12.7\sqrt{(f_P/8)}(Pr^{2/3}-1)} & \text{for } \begin{matrix} 3000 < Re < 5\cdot 10^6 \\ 0.5 < Pr \le 2000 \end{matrix} \\ 7.54 + \dfrac{0.03\cdot(D_h/L)Re\cdot Pr}{(D_h/L)Re\cdot Pr} & \text{for } \quad Re < 3000 \end{cases} \tag{B.2}$$

where f_P is the friction factor calculated by means of Petukhov equation, which according to [25] can be written as:

$$f_P = (0.790 \cdot \log Re - 1.64)^{-2} \tag{B.3}$$

For both regimes, the characteristic length L_C is equal to the hydraulic diameter, D_h [25]. The relation between D_h and the tube diameters is: $D_h = (D_{out} - D_{in})$. Thus, the hydraulic diameter can also be considered as two times the spacing of the plates (for the laminar regime). L represents the plate length, which, in this case, is assumed to be the Zone 1 length, $L1$. Therefore, the convection heat transfer coefficient, $h(T_{i1})$ is:

$$h_{i1} = h(T_{i1}) = \frac{Nu_{D_h}(Re, Pr) \cdot k_{air}(T_{i1})}{D_h} \tag{B.4}$$

The Nusselt number considered at the receiver output (phase 4 – o) was assumed to come from forced convection. If the flow is turbulent at the phase i – 1, it will be turbulent at this phase too and the Nusselt number will be the one employed for the annular tube. Actually, Cengel [25] outlines that for a turbulent flow within an annular geometry, Nusselt numbers for the inner and outer flows are approximately the same ($Nu_{Dh,inner} = Nu_{Dh,outer}$). On the contrary,

Table A.7
REFPROP-Mathematica® coefficients for dry air. Units in all coefficients are SI.

Dry air	a	b	c	d	e	f
c_p (J/ (kg K))	1068.53	−0.5252	$1.338{\cdot}10^{-3}$	$-1.031{\cdot}10^{-6}$	$3.208{\cdot}10^{-10}$	$-2.908{\cdot}10^{-14}$
k_{air} (W/m K)	$-4.457\cdot10^{-4}$	$1.089{\cdot}10^{-4}$	$-8.1629{\cdot}10^{-8}$	$6.323{\cdot}10^{-11}$	$-2.734{\cdot}10^{-14}$	$4.944{\cdot}10^{-18}$
μ (Pa)	$2.374{\cdot}10^{-8}$	$7.740{\cdot}10^{-8}$	$-6.885{\cdot}10^{-11}$	$5.362{\cdot}10^{-14}$	$-2.338{\cdot}10^{-17}$	$4.256{\cdot}10^{-21}$

if the flow at the phase i –1 is laminar, the flow at this stage will be also considered laminar, and the Nusselt number will be assumed as a flow over a flat plate since the diameter is higher than the tube length ($D_f > L1$). Hence, the Nusselt number for turbulent and laminar flows are:

$$Nu_{4o} = \begin{cases} Nu_{D_h}(Re,Pr) = \frac{(f_P/8)\cdot(Re-1000)\cdot Pr}{1+12.7\sqrt{(f_P/8)}(Pr^{2/3}-1)} & \text{for } \begin{matrix}3000 < Re < 5\cdot10^6\\ 0.5 < Pr \le 2000\end{matrix} \\ Nu_{L1}(Re,Pr) = 0.664\cdot Re^{0.5}\cdot Pr^{1/3} & \text{for } \begin{matrix}Re < 3000\\ Pr > 0.6\end{matrix} \end{cases} \tag{B.5}$$

Thus, the convection heat transfer coefficient, h_{4o} for a turbulent flow would be:

$$h_{4o} = h(T_{4o}) = \frac{Nu_{D_h}(Re,Pr)\cdot k_{air}(T_{i1})}{D_h} \tag{B.6}$$

while the expression for a laminar regime will be written as:

$$h_{4o} = h(T_{4o}) = \frac{Nu_{L1}(Re,Pr)\cdot k_{air}(T_{4o})}{L1} \tag{B.7}$$

B.2. Zone 2

Here, it is important to note that a uniform wall temperature was fixed for both faces, T_w. Hence, the heat exchange is assumed to occur from an isothermal surface. It was not considered a net flux flowing from phase 3 – 3B to phase 1 – 2, since $\Delta T = 0$. Therefore, the heat transfer coefficient will not be calculated as in Eq. (4), since it cannot be considered as the sum of 3 parallel thermal resistances. The Nusselt number considered here will be the one regarding the heat exchange between two parallel plates. Hence, the convective heat transfer at this Zone 2 is:

$$h_{wo} = h(T_{1w}) = \frac{Nu_{D_h}(Re,Pr)\cdot k_{air}(T_{1w})}{D_h} \tag{B.8}$$

where $Nu_{D_h}(Re,Pr)$ is the same Nusselt number correlation than the one expressed in Eq. (B.2). It is necessary to replace $L1$ by longitude $L2$, since the latter is the plate length for zone 2.

B.3. Zone 3

In this zone, there is a heat exchange between the fluid and the glass window, which will be treated as a vertical flat plate. There are two processes that can be described by means of the Nusselt correlations: forced convection at the inner glass surface and natural convection at the outer glass surface.

In the first one, the air flows over a flat circular plate. Thus, the Nusselt correlations employed for describing the turbulent and laminar flows are [25]:

$$Nu_{3-in} = \begin{cases} Nu_{r_g}(Re,Pr) = 0.037\cdot Re^{0.8}\cdot Pr^{1/3} & \text{for } \begin{matrix}5\cdot10^5 < Re < 10^7\\ Pr > 0.6\end{matrix} \\ Nu_{r_g}(Re,Pr) = 0.664\cdot Re^{0.5}\cdot Pr^{1/3} & \text{for } \begin{matrix}Re < 5\cdot10^5\\ Pr > 0.6\end{matrix} \end{cases} \tag{B.9}$$

Hence, the convective heat transfer at the inner quartz glass surface is:

$$h_{gi} = h(T_{3gi}) = \frac{Nu_{r_g}(Re,Pr)\cdot k_{air}(T_{gi3})}{r_g} \tag{B.10}$$

where the characteristic length is the glass radius, r_g, because of the radial symmetry of the air flux when hitting the window.

At the outer glass surface, the Nusselt correlation considered is natural convection over a flat vertical plate [25]:

$$Nu_{3-out} = Nu_{\sqrt{Ag}}(Ra,Pr) = \left(0.825 + \frac{0.387Ra^{(1/6)}}{\left[1+(0.492/Pr)^{9/16}\right]^{8/27}}\right)^2 \quad \text{for } \begin{matrix}Re < 3000\\ Pr > 0.6\end{matrix} \tag{B.11}$$

where the characteristic length here is the squared root of the glass window area, $\sqrt{A_g}$. The Rayleigh number (Ra) is defined in terms of the Grashof number, Gr, and Prandtl number:

$$Ra = Gr\cdot Pr = \frac{g\,\beta\,(T_{go}-T_a)(\sqrt{A_g})^3}{(\mu/\rho)^2}\cdot Pr \tag{B.12}$$

where g is the acceleration of gravity, β is the coefficient of volume expansion at mean temperature, $\beta = 1/(0.5(T_{go}+T_a))$, and μ and ρ are the fluid dynamic viscosity and density, respectively.

B.4. Zone 3B

After hitting the glass window, the air goes towards the absorbing foam through the inner wall surface. Since Zone 1 geometry can be applied here, the Nusselt correlation is the same as the one employed for phase 4-o [see Eq. (B.9)]:

$$Nu_{win} = Nu_{4o} \tag{B.13}$$

Within zone 3B, it is necessary to substitute $L1$ with $L2$, because the latter is the inner wall cylinder length.

B.5. Zone 4

Here, the fluid flows across the porous absorbing foam. This element is crucial within the receiver systems since it provides the most significant heat flux to the air. The calculation of its convective heat transfer coefficient differs from the previous ones since it will be obtained for a volume instead of a surface. The volumetric heat transfer coefficient, h_v, for this work was computed by following Zhu et al. [14], Barreto et al. [30], Wu et al. [31] and Viskanta et al. [29] publications. According to Barreto et al. [30] and Wu et al. [31], the Nusselt correlation for a porous medium like this metal foam, can be expressed as:

$$Nu_v = (32.504\phi^{0.38} - 109.94\phi^{1.38} + 166.65\phi^{2.38} - 86.98\phi^{3.38})\,Re_{d_c}^{0.438} \tag{B.14}$$

For such a complex geometry like a porous medium, this Nusselt correlation allows obtaining h_v in terms of the porosity, ϵ, and the Reynolds number based on the average pore cell diameter, d_c:

$$Re_{d_c} = \frac{\rho\,\phi^2\,u\,d_c}{\mu} \tag{B.15}$$

where the product $\phi^2\,v$ accounts for the module of the superficial velocity, while u represents the mean velocity in the pores.

Zhu's work provides some information on the metal foam characteristics: Pores per Inch (PPI) and pore diameter, d_p. However, parameters

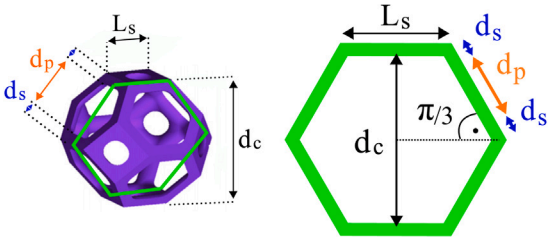

Fig. B.8. Scheme for the estimation of the strut length, L_s, strut diameter, d_s and average cell diameter, d_c.
Source: Adapted from Wu et al. [31].

like porosity, ϕ, and average pore cell diameter, d_c, were obtained by using the relations described in the next paragraph. Note that the study of this kind of porous media is not simple and, as Fu et al. [29] mention within their work, '*for a given PPI, the actual pore diameter varies greatly among materials, even samples of the same material supplied by the same manufacturer show differences in the actual pore diameter*'. The porosity, ϕ, was obtained by following the expression [29]:

$$d_p = \frac{\sqrt{\frac{4\phi}{\pi}}}{PPm} \rightarrow \phi = \frac{\pi}{4}\left(PPm \cdot d_p\right)^2 \tag{B.16}$$

where PPm are the number of pores per meter ($PPm = \frac{PPI}{0.0254\,\mathrm{m/in}}$). From the porosity, the cell diameter (d_c) can be calculated from Wu et al. [31] expressions:

$$d_c = 2.828 L_s \tag{B.17}$$

$$\phi = 1 - \frac{9.425}{8\sqrt{2}}\left(\frac{d_s}{L_s}\right)^2 + \frac{3.33}{8\sqrt{2}}\left(\frac{d_s}{L_s}\right)^3 \tag{B.18}$$

Besides, a geometric approximation was done in order to have another relation between L_s and d_s:

$$\sin\left(\frac{\pi}{3}\right) = \frac{d_c/2}{2d_s + d_p} \rightarrow \sin\left(\frac{\pi}{3}\right) = \frac{2.828 L_s}{2(2d_s + d_p)} \tag{B.19}$$

where d_s is the strut diameter and L_s is the strut length. Aiming to explain Eq. (B.19), a scheme of the cell geometry considered is presented in Fig. B.8. Although the cell geometry follows a packed tetrakaidecahedra structure [31], the cross section considered here is a regular hexagon. Thus, the relation among d_s, l_s and d_c can be obtained by using a simple trigonometric relation.

Appendix C. View factors F_{ij}

The view factors exposed in Table 5 were calculated from the glass window and porous foam aperture areas, A_g and A_f, respectively. The effective inner wall area, A_w, was also considered. These parameters are clearly described within Zhu et al. [14] work. Thus, the 'glass to foam' view factor, F_{gf}, is obtained by following Cengel [25] and Kalogirou [27] expressions for coaxial parallel disks:

$$R_1 = \frac{r_g}{a}; \qquad R_2 = \frac{r_f}{a}; \qquad a = L_2 + 0.01 \tag{C.1}$$

$$X = 1 + \frac{1 + R_2^2}{R_1^2} \tag{C.2}$$

$$F_{gf} = \frac{1}{2}\left(X - \sqrt{X^2 - 4\left(\frac{R_2}{R_1}\right)^2}\right) \tag{C.3}$$

where a is the distance between the glass window and porous foam disks and L_2 is the receiver length for phase 1–2 (to the left of the foam) (See Table 6). It has been considered a 1 cm separation between the glass window plane and the inner wall cylinder plane (see Fig. 1(b) for better understanding). Once F_{gf} is obtained, the 'foam to glass' view factor, F_{fg}, is calculated by means of the reciprocity relation for view factors:

$$A_f F_{fg} = A_g F_{gf} \rightarrow F_{fg} = \frac{A_g}{A_f} F_{gf} \tag{C.4}$$

The 'glass to wall' view factor, F_{gw}, can be obtained by means of the summation rule. The conservation of energy through the summation rule establishes that *the sum of the view factors from surface 'i' of an enclosure to all surfaces of the enclosure, including to itself, must equal unity* [25]. Assuming that the glass window does not reflect any radiation onto it itself (*i.e.*, $F_{gg} = 0$), the summation rule here can be described as:

$$F_{gw} + F_{gf} = 1 \rightarrow F_{gw} = 1 - F_{gf} \tag{C.5}$$

Following the same relation, the 'foam to wall', F_{fw} view factor can be calculated:

$$F_{fg} + F_{fw} = 1 \rightarrow F_{fw} = 1 - F_{fg} \tag{C.6}$$

The 'wall to glass' (F_{wg}) and 'wall to foam' (F_{wf}) view factors can be obtained once the effective wall area, A_w, is known. The inner wall is a cylinder which has on the left an aperture equal to the glass window surface, and on the right is placed the porous foam. Thus, A_w is the sum of an outer ring surface and a cylindrical surface:

$$A_w = \pi(r_f^2 - r_g^2) + 2\pi r_f L_2 \tag{C.7}$$

The reciprocity rule allows to obtain the 'wall to glass' (F_{wg}) and 'wall to foam' (F_{wf}) view factors:

$$F_{wg} = \frac{A_g}{A_w} F_{gw} \tag{C.8}$$

$$F_{wf} = \frac{A_f}{A_w} F_{fw} \tag{C.9}$$

Since part of the inner wall surface is normal to the surface itself, there exists a non-zero 'wall to wall' view factor, F_{ww}. Although F_{ww} does not appear within the receiver model set of equations, it can be also calculated through the summation rule:

$$F_{ww} = 1 - F_{wf} - F_{wg} \tag{C.10}$$

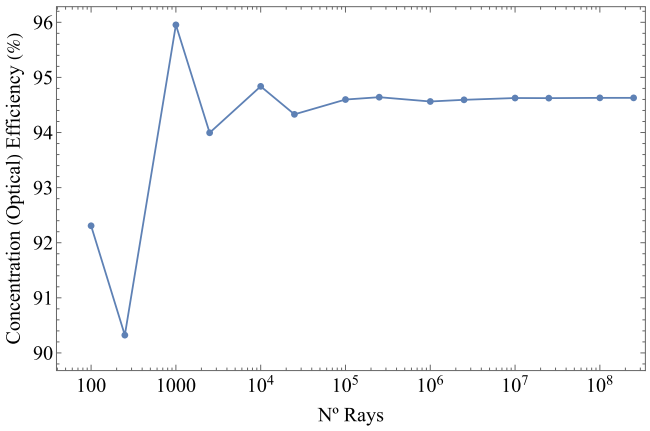

Fig. D.9. Optical efficiency, η_{opt}, obtained in Tonatiuh software as a function of the number of rays. It corresponds to the PDC with CF = 100 (see Table 3).

Appendix D. Optical efficiency validation details.

This appendix serves as an extension of the Tonatiuh validation process exposed in Section 3. Apart from the comparison of the optical efficiency itself, η_{opt}, (see Table 3) with the results by Barreto and Canhoto [2], a comparison between the radiation flux over the receiver

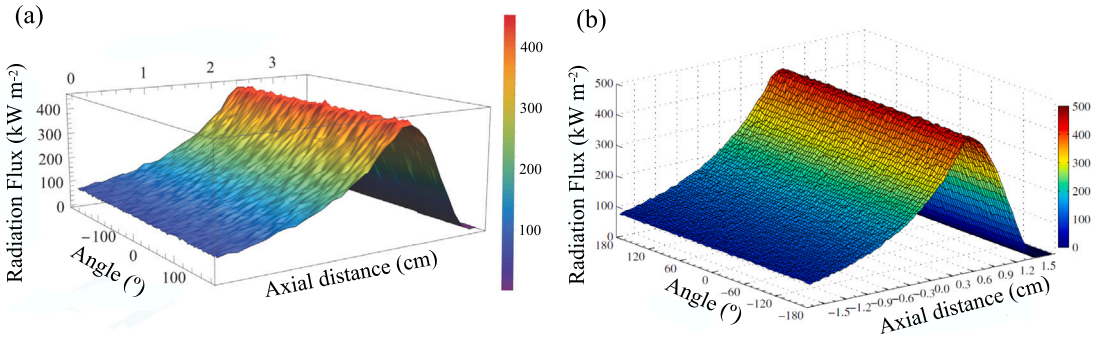

Fig. D.10. Radiation flux over the receiver cylindrical surface placed at the focus of the PDC with CF = 250 (See Table 3): (a) This work, (b) Barreto and Canhoto's [2] work.

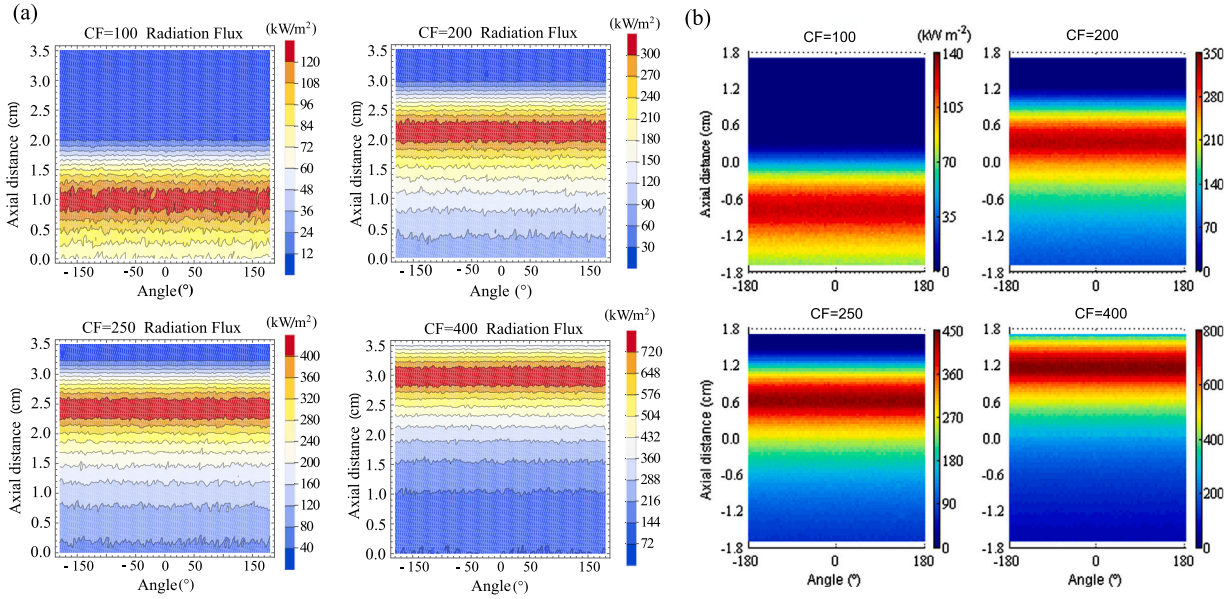

Fig. D.11. Radiation flux in the cylindrical surface of the receiver for different concentration factors: (a) This work and (b) Barreto and Canhoto's [2] work.

cylindrical surface was also performed. The number of rays selected for the validation process (25 million) is also justified in the following subsection.

D.1. Influence of the ray number

Barreto and Canhoto [2] used 250 million rays for simulating the optical subsystem of the PDC in Tonatiuh software. Due to computational time reasons, the validation of the Mathematica®, code employed for post-processing the results in this work, could not be done with such a large number of rays. Thus, in Fig. D.9, the optical efficiency, η_{opt}, obtained in Tonatiuh is depicted as a function of the number of rays. Those simulations were done for the concentration system with a CF = 100. As it is seen in Table 3, the optical efficiency for that dish is 94.60%.

According to Fig. D.9, it seems that from 1 million ray number, η_{opt} tends to be stable and it changes from 94.58% for 1 million rays, up to 94.65% for 250 million rays. Thus, as mentioned in Section 3, the validation process was carried out with a 25 million ray number aiming to lower the computational time.

D.2. Radiation flux in the receiver cylindrical surface

The distribution of the energy flux along the receiver's cylindrical surface (see Fig. 2) is shown in Fig. D.10. The concentration factor selected is CF = 250. The axial distance in this work (Fig. D.10(a)) is represented with reference to the bottom cylinder basis (facing the PDC collector). Thus, an axial distance equal to 0 cm represents the bottom basis and an axial distance of 3.51 cm represents the cylinder top basis. On the contrary, Barreto and Canhoto (Fig. D.10(b)) [2] take the middle of the cylinder as a reference for the axial distance. The maximum energy flux (400–420 kW/m^2) is registered over the ring placed at 2.5 cm from the basis (or at 0.7 cm from the middle, according to Barreto and Canhoto's work [2]). For the parabolic dish of CF = 250, the solar radiation does not hit the top of the cylinder, so the energy flux at 3.51 cm from the bottom (or at 1.76 cm for Barreto and Canhoto's work) is zero.

The plane projection is depicted in Fig. D.11 for analyzing and comparing the other concentration factors. The difference in the axial distance scale between Fig. D.11(a) and (b) was already explained for Fig. D.10. In this work (Fig. D.11(a)), as well as in Barreto and Canhoto's work (Fig. D.11(b)), it is clear that the higher the CF is, the further axial distance for the maximum energy flux is achieved. Besides, the energy flux also raises with higher concentration factors. For a CF = 100, the maximum energy flux (120 kW/m^2) is obtained at 1 cm from the bottom basis (−0.7cm for Barreto and Canhoto's reference). For the maximum CF analyzed (CF = 400), the maximum energy flux (above 720 kW/m^2) is obtained at 3 cm from the bottom basis (1.2 cm for Barreto and Canhoto's).

Finally, in Fig. D.12, the integrated radiation flux as a function of the axial distance is shown for the different concentration factors. Both radiation flux and axial distance are turned into dimensionless

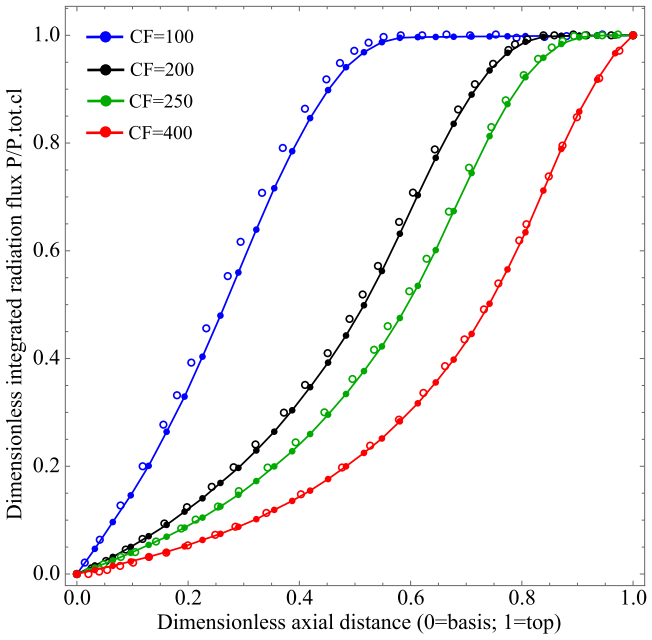

Fig. D.12. Dimensionless integrated radiation flux in the cylindrical receiver surface as a function of the dimensionless axial distance for CF = 100 (blue), CF = 200 (black), CF = 250 (green) and CF = 400 (red): Solid lines with filled markers, this work and empty markers, Barreto and Canhoto's [2] work.

variables. The vertical axis represents the integral of the flux for each axial distance with respect to the total amount of energy received at the cylindrical receiver surface. Similarly to Fig. D.11, it is seen that for lower values of CF, the maximum of the energy flux is attained at lower axial distances. As Barreto and Canhoto establish, the most uniform energy distribution is obtained for CF = 250 (green line and markers in Fig. D.12). For CF = 100 (blue lines in Fig. D.12), the energy flux is concentrated in the first bottom-to-middle cylindrical surface, while for the higher concentration factor (CF = 400, red plots in Fig. D.12), the maximum energy flux is located at the top of the cylinder.

Thus, from all the results shown, it can be considered that the developed Mathematica® software for the post-processing of the results obtained with Tonatiuh has been further validated.

References

[1] Coventry J, Andraka C. Dish systems for CSP. Sol Energy 2017;152:140–70.

[2] Barreto G, Canhoto P. Modelling of a Stirling engine with parabolic dish for thermal to electric conversion of solar energy. Energy Convers Manage 2017;132:119–35. http://dx.doi.org/10.1016/j.enconman.2016.11.011.

[3] Blanco MJ, Amieva JM, Mancillas A. The Tonatiuh software development project: An open source approach to the simulation of solar concentrating systems. In: ASME 2005 international mechanical engineering congress and exposition. American Society of Mechanical Engineers; 2005, p. 157–64.

[4] Sedighi M, Vasquez Padilla R, Taylor R, Lake M, Izadgoshasb I, Rose A. High-temperature, point-focus, pressurised gas-phase solar receivers: A comprehensive review. Energy Convers Manage 2019;185:678–717. http://dx.doi.org/10.1016/j.enconman.2019.02.020.

[5] Aichmayer L, Garrido J, Laumert B. Thermo-mechanical solar receiver design and validation for a microgas-turbine based solar dish system. Energy 2020;196:116929.

[6] Merchán RP, Santos MJ, Medina A, Calvo Hernández A. High temperature central tower plants for concentrated solar power: 2021 overview. Renew Sustain Energy Rev 2022;155:111828. http://dx.doi.org/10.1016/j.rser.2021.111828.

[7] Lubkoll M, von Backström T, Kröger D. Survey on pressurized air receiver development. In: Sol. ener. conference. 2014, http://sterg.sun.ac.za/wp-content/uploads/2018/07/Lubkoll-501.pdf.

[8] Wang W, Malmquist A, Laumert B. Comparison of potential control strategies for an impinging reciver based dish-brayton system when the solar irradiation exceeds its design value. Energy Convers Manage 2018;169:1–12.

[9] Mohammadi A, Mehrpooya M. Exergy analysis and optimization of an integrated micro gas turbine, compressed air energy storate and solar dish collector process. J Clean Prod 2016;139:372–83.

[10] Dua Zhao, Liua Gang, Huanga Xinyu, Xiaob Tian, Yanga Xiaohu, Hec Ya-Ling. Numerical studies on a fin-foam composite structure towards improving melting phase change. Int J Heat Mass Transfer 2023;208:124076.

[11] Li Fangfei, Huang Xinyu, Li Yuanji, Lu Liu, Meng Xiangzhao, Yang Xiaohu, et al. Application and analysis of flip mechanism in the melting process of a triplex-tube latent heat energy storage unit. Energy Rep 2023;9:3989–4004.

[12] Zhu J, Wang K, Li G, Wu H, Jiang Z, Lin F, et al. Experimental study of the energy and exergy performance for a pressurized volumetric solar receiver. Appl Therm Eng 2016;104:212–21. http://dx.doi.org/10.1016/j.applthermaleng.2016.05.075.

[13] Patil VR, Kiener F, Grylka A, Steinfeld A. Experimental testing of a solar air cavity-receiver with reticulated porous ceramic absorbers for thermal processing at above 1000°C. Sol Energy 2021;214:72–85. http://dx.doi.org/10.1016/j.solener.2020.11.045.

[14] Zhu J, Wang K, Jiang Z, Zhua B, Wu H. Modeling of heat transfer for energy efficiency prediction of solar receivers. Energy 2020;190:116372. http://dx.doi.org/10.1016/j.energy.2019.116372, https://www.sciencedirect.com/science/article/pii/S0360544219320675.

[15] Bellos E, Bousi E, Tzivanidis C, Pavlovic S. Optical and thermal analysis of different cavity receiver designs for solar dish concentrators. Energy Convers Manage X 2019;2:100013. http://dx.doi.org/10.1016/j.ecmx.2019.100013.

[16] Kasaeian A, Kouravand A, Vaziri Rad MA, Maniee S, Porufayaz F. Cavity receivers in solar dish collectors: A geometric overview. Renew Energy 2021;169:53–79. http://dx.doi.org/10.1016/j.renene.2020.12.106.

[17] Wang P, Li JB, Bai FW, Liu DY, Xu C, Zhao L, et al. Experimental and theoretical evaluation on the thermal performance of a windowed volumetric solar receiver. Energy 2017;119:652–61. http://dx.doi.org/10.1016/j.energy.2016.11.0240360-5442.

[18] Sharma S, Talukdar P. Thermo-mechanical analysis of a porous volumetric solar receiver subjected to concentrated solar radiation. Sol Energy 2022;247:41–54. http://dx.doi.org/10.1016/j.solener.2022.10.014.

[19] Craig KJ, Slootweg M, Le Roux WG, Wolff TM, Meyer JP. Using CFD and ray tracing to estimate the heat losses of a tubular cavity dish receiver for different inclination angles. Sol Energy 2020;211:1137–58. http://dx.doi.org/10.1016/j.solener.2020.10.054.

[20] Semprini S, Sánchez D, De Pascale A. Performance analysis of a micro gas turbine and solar dish integrated system under different solar-only and hybrid operating conditions. Sol Energy 2016;132:279–93.

[21] Lanchi M, Al-Zaili J, Russo V, Falchetta M, Montecchi M, Aichmayer L. A quasi-steady state model of a solar parabolic dish micro gas turbine demonstration plant. Energies 2022. http://dx.doi.org/10.3390/en15031059.

[22] Inc. WR. Mathematica, version 13.2. Champaign, IL; 2022, https://www.wolfram.com/mathematica.

[23] Giostri A, Macchi E. An advanced solution to boost sun-to-electricity efficiency of parabolic dish. Sol Energy 2016;139:337–54. http://dx.doi.org/10.1016/j.solener.2016.10.001.

[24] Blanco MJ, Mutuberria A, Martinez D. Experimental validation of Tonatiuh using the Plataforma Solar de Almería secondary concentrator test campaign data. In: 16th Annual SolarPACES symposium. 2010.

[25] Cengel YA, Ghajar AJ. Heat and mass transfer: Fundamentals and applications. 5th ed. McGraw-Hill Professional; 2014.

[26] Lemmon EW, Huber ML, McLinden MO. NIST standard reference database 23: Reference fluid thermodynamic and transport properties-REFPROP, version 9.1. Gaithersburg: National Institute of Standards and Technology, Standard Reference Data Program; 2013.

[27] Kalogirou SA. Solar energy engineering: Processes and systems. 2nd ed. 2014.

[28] Modest MF. Radiative heat transfer. 2nd ed. Academic Press, Elsevier Science; 2003.

[29] Fu X, Viskanta R, Gore J. Measurement and correlation of volumetric heat transfer coefficients of cellular ceramics. Exp Therm Fluid Sci 1998;17:285–93. http://dx.doi.org/10.1016/S0894-1777(98)10002-X.

[30] Barreto G, Canhoto P, Collares-Pereira M. Three-dimensional CFD modelling and thermal performance analysis of porous volumetric receivers coupled to solar concentration systems. Appl Energy 2019;252:113433. http://dx.doi.org/10.1016/j.apenergy.2019.113433, https://www.sciencedirect.com/science/article/pii/S0306261919311079.

[31] Wu Z, Caliot C, Flamant G, Wang Z. Numerical simulation of convective heat transfer between air flow and ceramic foams to optimise volumetric solar air receiver performances. Int J Heat Mass Transfer 2011;54(7–8):1527–37. http://dx.doi.org/10.1016/j.ijheatmasstransfer.2010.11.037.

[32] Horta P, Osório T. Optical characterization parameters for line-focusing solar concentrators: Measurement procedures and extended simulation results. Energy Procedia 2014;49:98–108. http://dx.doi.org/10.1016/j.egypro.2014.03.011.

[33] Tutorial ParabolicDish V201. 2021, https://github.com/iat-cener/tonatiuh/wiki/Tutorial-ParabolicDish-V201. [Accessed on 06 February 2023].

[34] Group WB. Morocco - Noor-Ouarzazate concentrated solar power plant project. Washington, D.C.: World Bank Group (English) http://documents.worldbank.org/curated/en/748641468279941398/Morocco-Noor-Ouarzazate-Concentrated-Solar-Power-Plant-Project.

[35] García-Ferrero J, Merchán RP, Santos MJ, Medina A, Calvo Hernández A. Brayton technology for concentrated solar power plants: Comparative analysis of central tower plants and parabolic dish farms. Energy Convers Manage 2022;271:116312. http://dx.doi.org/10.1016/j.enconman.2022.116312.

[36] Global Modeling and Assimilation Office (GMAO). MERRA-2 Tavg1_2d_slv_Nx: 2d, 1-hourly, time-averaged, single-level, assimilation, single-level diagnostics V5.12.4. Greenbelt, MD, USA: Goddard Earth Sciences Data and Information Services Center (GES DISC); 2015, http://dx.doi.org/10.5067/VJAFPLI1CSIV, https://www.soda-pro.com/web-services/meteo-data/merra. [Accessed 23 February 2023].

[37] Copernicus atmosphere monitoring service (ECMWF). 2023, https://www.soda-pro.com/web-services/radiation/cams-radiation-service. [Accessed 23 February 2023].

[38] García-Ferrero J, Heras I, Santos M, Merchán R, Medina A, González A, et al. Thermodynamic and cost analysis of a solar dish power plant in spain hybridized with a micro-gas turbine. Energies 2020;13:5178. http://dx.doi.org/10.3390/en13195178.

[39] Kipp Zonen. [link]. https://www.kippzonen.com/Product/281/SMP10-Pyranometer#.ZEZkTy3Wd0I.

[40] Lufft. User manual: Smart weather sensor WS10. Lufft WS10, https://www.lufft.com/.

[41] Hassan OH, Sultan GI, Sabry MN, Hegazi AA. Investigation of heat transfer and pressure drop in a porous media with internal heat generation. Case Stud Therm Eng 2022;32:101849. http://dx.doi.org/10.1016/j.csite.2022.101849.